Journal Pre-proof

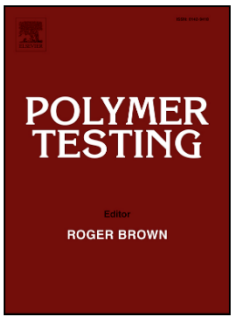

Development and Validation of a mechanistic model for the release of embelin from a polycaprolactone matrix

Irene T. Seoane, Pablo R. Cortez Tornello, Leonel Silva, J. Pablo Tomba, Gustavo A. Abraham, Adrián Cisilino

PII: S0142-9418(20)32084-5

DOI: https://doi.org/10.1016/j.polymertesting.2020.106855

Reference: POTE 106855

To appear in: *Polymer Testing*

Received Date: 15 May 2020

Revised Date: 26 August 2020

Accepted Date: 11 September 2020

Please cite this article as: I.T. Seoane, P.R. Cortez Tornello, L. Silva, J.P. Tomba, G.A. Abraham, A. Cisilino, Development and Validation of a mechanistic model for the release of embelin from a polycaprolactone matrix, *Polymer Testing*, https://doi.org/10.1016/j.polymertesting.2020.106855.

DEVELOPMENT AND VALIDATION OF A MECHANISTIC MODEL FOR THE RELEASE OF EMBELIN FROM A POLYCAPROLACTONE MATRIX

Irene T. Seoane*, Pablo R. Cortez Tornello, Leonel Silva, J. Pablo Tomba, Gustavo A. Abraham and Adrián Cisilino

Instituto de Investigaciones en Ciencia y Tecnología de Materiales (INTEMA), UNMdP-CONICET, Facultad de Ingeniería, Av. Juan B Justo 4302, 7600 Mar del Plata, Argentina.

*Corresponding author: *itseoane@fi.mdp.edu.ar*

Abstract. Embelin is a natural agent with antimicrobial, antifungal and analgesic activities. This work presents a mechanistic model for the release of embelin from a polycaprolactone matrix. Based on the results of embelin release experiments and Raman microscopy measurements, the model assumes a dual dispersion of the embelin: agglomerated and dispersed. Embelin release mechanism combines the effects of the liquid migration into the matrix, the drug diffusion, and the drug dissolution within the wetted matrix. The model is formulated in terms of four partial differential equations that account for the mass balances of dispersed, agglomerated, and dissolved embelin, and aqueous solution. Model predictions show that the release mechanism involves three stages: a burst stage, in which dispersed embelin is rapidly released; a transition stage, in which dispersed and agglomerated embelin are simultaneously released; and, once the dispersed embelin depletion, a stable release stage until the agglomerated embelin exhausts.

Keywords: Mechanistic Model, Drug Release, Polycaprolactone, Embelin.

1 Introduction

Controlled drug delivery systems are efficient, versatile and safe means for the pharmacological treatment of a number of human diseases [1,2]. Controlled drug delivery technology facilitates the transport of a pharmaceutical agent to a specific area of the body and assures the release of the agent into a therapeutic level for a sustained period of time [3]. Therefore, drug delivery systems contribute to control the biodistribution and to increase the bioavailability of therapeutic agents [4].

Embelin is a natural benzoquinone therapeutic agent with poor water solubility. Embelin can be isolated from species of the *Myrsinaceae* and *Oxalidaceae* families and has diverse biological properties, including antimicrobial, antifungal, and analgesic activities [5–7]. It has been observed that poly(ε-caprolactone) (PCL) scaffolds containing embelin presented

biocompatible, biodegradable, semicrystalline and hydrophobic polyester extensively used in drug delivery systems due to its good drug permeability and low degradation rate [10,11]. A number of embelin-loaded PCL systems have been studied and proposed by our group [12–14]. Being hydrophobic and degradation resistant, the penetration of aqueous solutions into and through PCL devices are minimal, what results in reduced drug release rates [15,16]. Thus, drug doses can be controlled, the administration frequency reduced, while the possibility of overdose is erased.

So far, embelin release from PCL matrices has been studied by using empirical mathematical models, like zero-order and Korsmeyer-Peppas' models [12]. The zero-order model, in which the drug release rate remains constant over time, provides a good fit of experimental data during the initial burst release stage, but it fails for the subsequent release stages. The Korsmeyer-Peppas model proposes a power-law dependence of the drug release with time, so it can be either used to fit the burst stage (in such a case, it reduces to the zero order model) or the long-term release (assuming quasi-Fickian diffusion). However, this model is unable to describe the complete behavior in a unified way. The limitations of the above models to describe the embelin release phenomena in a unified way suggest that multiple mechanisms of drug transport and release might take part simultaneously [9].

Mechanistic mathematical descriptions of mass transport in controlled drug delivery systems allow for deeper insights into the phenomena involved in drug release. In contrast to empirical and semi-empirical models, mechanistic models incorporate the physical, chemical and/or biological phenomena of the system [17]. Mechanistic models are effective to help in the design and tuning of drug delivery systems by accelerating developing times and reducing time- and cost-intensive series of trial-and-error experiments [18,19].

Diffusional mass transport is an important limitation to drug release in delivery systems [20]. Drug diffusion could control the delivery rate or it could be predominant in combination with other mechanisms such as drug dissolution, polymer swelling or polymer degradation [21]. Additional phenomena to consider are fluid penetration, initial spatial drug distribution, drug solubility and drug crystallinity.

The model by Higuchi [22] is the most extended to study diffusion-controlled non-degrading systems in which the initial drug concentration exceeds drug solubility in the wetted system [23]. Higuchi's model assumes that the liquid penetrates rapidly into the system, that the partial dissolution of the drug assures a saturated solution, and that only dissolved drug is able to diffuse according to Fick's law. In practice, this results in a model in which the system empties starting from the outermost exposed layers and progresses towards the interior layers. The embelin-PCL system has two characteristics that make it incompatible with Higuchi's model: hydrophobic character of PCL prevents the rapid penetration of the liquid into the system, and the embelin dissolution rate is slow in comparison to its diffusion velocity in the liquid.

This work introduces a mechanistic model for the release of embelin from PCL films that

level. The model accounts for the combined effects of the diffusion of the liquid into the system, the dissolution of embelin in the wetted matrix and the diffusion of the dissolved embelin in the liquid. The model formulation is based on the results of embelin release experiments and Raman microscopy measurements. Raman microscopy is used to characterize the in-depth embelin spatial distribution, which is a key data for the model development.

2 Materials

Embelin (2.5-dihydroxy-3-undecil-1.4-benzoquinone, Fig. 1a) was isolated from *Oxalis erythrorhiza* Gillies ex Hooker et Arnott (*Oxaloacetate*) that was collected in San Juan province (Argentina) following the procedure described by Feresin et al. [24]. Embelin density is 1.130 $g \cdot cm^{-3}$. PCL (number-average molecular weight of 80.000 $g \cdot mol^{-1}$ and density 1.145 $g \cdot cm^{-3}$), dichloromethane (DCM) and N,N-dimethylformamide (DMF) were purchased from Aldrich Chemical Co. (St Louis, MO, USA). PCL chemical structure is shown in Fig. 1b.

3 Experimental

3.1 Preparation of embelin-loaded PCL films

PCL matrices were prepared by solvent casting. A predetermined amount of PCL pellets were dissolved in 5 ml of DCM:DMF mixture (1:1 by volume) under stirring to obtain a polymer concentration of 10 wt%. Embelin were then added to the solution at 3 wt% and 18 wt%. Embelin amounts were selected to assure the minimum inhibitory concentration index (MIC) for the films to be effective delivery systems with bactericidal and trypanocidal activity [12]. The 3 wt% is intended to obtain films in which embelin is most dissolved in the PCL matrix; the 18 wt% is intended to achieve the degree of drug saturation in the films.

The solutions were poured into a 4.6 cm-diameter Petri dish (Fig. 1c) and dried under a fume hood for 24 h at room temperature to obtain films, which were labelled E3 and E18 according to their embelin loads. Films were then dried in a vacuum oven to remove the residual solvent. Films were homogeneous and opaque, with the typical aspect of PCL films. Film thicknesses, e=700 ± 150 ∝m, were measured with a low force caliper. Films were stored at room temperature for 45 days to ensure a constant crystallization degree for PCL before pursuing any test.

3.2 Porosity

Liquid extrusion porosimetry (LEP) was used to determine the film porosity. Vaseline (surface tension γ = 33 dyn cm^{-1}) was used as intrusion liquid because it spontaneously fills the porous structures of PCL (contact angle near to zero) without swelling effects [13]. Test

USA). LEP measurements were complemented with scanning electron microscopy (SEM) observations to characterize the surface porosity and morphology. Samples were examined using a JEOL JSM-6460LV microscope after gold sputtering. Surface porosity was also measured from SEM micrographs using the software ImageJ.

3.3 Embelin quantification and distribution

Embelin content of the films was measured using ultraviolet-visible spectroscopy (Agilent 8453). Disc samples with 3 mm in diameter were cut from the films and were dissolved in the DCM:DMF mixture, and quantification was carried out after calibration, observing the absorption band at λ = 330 nm, in accordance with the procedure by Prasad et al. [25]. Calibration resulted with $R^2 = 0.989$.

Distributions of embelin and PCL throughout the film thickness were probed with a confocal Raman microscope (Renishaw InVia Reflex). This equipment consists of a Leica DM2500 microscope, optically attached to a charge-coupled device (CCD) with a detector of 1024×256 pixels for the spectral and spatial dimensions. A laser excitation of 785 nm was used in combination with a grating of 1200 grooves·mm^{-1}. Regular confocality was used in all the measurements. Raman profiles were obtained by two ways: in-depth and laterally (both along the z-axis), as shown in Fig. 1d. Lateral profiles were measured along paths on the exposed, previously cut, lateral surface of the film, from the top to the bottom of the sample. Measurements were performed using a metallurgical Leica ×50 (NA=0.75) microscope objective in steps of 100 µm, an exposure time of 2 seconds per spectrum and 4 accumulations. Lateral profiles provide a qualitative mapping of the embelin content across the complete specimen thickness. In-depth profiling was used to examine non-invasively and without cutting, the top and bottom surfaces of the sample, up to depths of about 50 µm. Measurements were carried out using a Leica ×100 (NA=1.3) objective with oil-immersion optics to preserve depth resolution. These spectra were acquired using 1 second per spectrum and 5 accumulations.

Linear spectral decomposition method was used to obtain individual contributions of embelin and PCL [26]. Thus, the Raman spectra of the film were decomposed into linear combinations of the pure PCL and the embelin spectra plus a polynomial that accounted for the changes in the baseline. The coefficients of the linear combinations represent the individual contributions of the components; the results for the embelin contribution are referred to as “embelin Raman intensity” hereafter. To compare the results of the model simulations with the experimental measurements, the embelin profiles by the model were convoluted with the theoretical Raman response; this was done following earlier works that account for the effects of the spot-size and attenuation of the laser beam on the in-depth profile [27,28].

3.4 Embelin release tests

(PBS, pH = 7.4) at 37 °C. Release measurements were made using 10 mm-diameter disc-shaped specimens extracted from E3 and E18 samples. Release tests consisted of ten specimens (with a mean initial total weight of 520 mg) placed into glass flasks containing 200 ml of solution that was stirred with an orbital shaker at 150 rpm for 18.5 days (Fig. 1e). The embelin content in the solution was periodically monitored. For this, a 1-ml aliquot (0.5% of the solution volume) was extracted from the solution every hour during the first 12 h, and every 24 h during the following 18 days. The extracted volumes were replaced with fresh solution. All measurements were conducted in triplicate and the results averaged. The concentration of released embelin was determined by ultraviolet-visible spectroscopy following the procedure explained in Section 3.3. Release tests lasted until embelin contents were completely depleted.

4 Results and Discussion

4.1 Embelin content

Actual embelin contents in the films were 2.9 wt% for E3 and 6.1 wt% for E18. In the latter case, a high fraction of embelin was rejected from a saturated PCL matrix as a fine powder that was easily removed from the film surface. Based on their embelin contents, the specimens extracted from the films were labelled eE3 and eE6, respectively.

4.2 Porosity

LEP tests reached a maximum applied pressure of $P_M = 20\,psi$ without vaseline going through the film. The estimation of the upper bound for the pore diameter by means of the Washburn's equation, $d_p = 4\gamma/P_M \cong 0.95\,\mu m$, resulted less than one micrometer [13]. Thus, the result of the LEP test can be attributed to the films to have pores smaller than a micrometer or to the absence of through-pores across the film.

Fig. 2 shows a SEM micrograph of the E3 surface. It can be observed that film surfaces present a high number of cavities which can be ascribed to a high surface porosity which is induced by a rapid volatilization of the solvent during casting and, probably, the addition of embelin [12]. Mean pore size in the surface is in the range from 5 μm to 10 μm, with a small number of large pores larger than 100 μm. On the other hand, observations of the samples prepared with 18 wt% of embelin showed that surface pores were completely full (and thus with no room for extra embelin), what is consistent with the exudation of the embelin excess reported in the previous section.

4.3 Embelin spatial distribution

Fig 3a shows the Raman spectra of pure embelin, pure PCL and that typical of an embelin-PCL film. It is seen that the spectral profiles of pure PCL and embelin are different. Therefore, these individual components can be well resolved in the composite spectra of the film. Fig. 3b depicts the embelin Raman intensity profiles resulting from the lateral

figure in the insert combines the data of the five measurements. Similar profiles were obtained for the specimen eE3. The intensity results allow to infer that embelin concentrations are nearly constant along most of the specimen thicknesses, with accumulations in the zones next to the specimen surfaces.

Fig. 4 presents the Raman intensity profiles of embelin in the zone next to the specimen surfaces (up to $50\,\mu m$ depth), as obtained from in-depth profiling measurements. The figure brings together the results of the measurements practiced on the top and bottom surfaces. In these plots, positive z-values correspond to focusing points above the sample surface, whereas negative values correspond to focusing points within the sample; the scale is zeroed at the position where the sample surface is in focus to be visually observed. The bell-shaped response profile shows that even when focusing above the sample surface, some signal arising from the sample interior is observed because of the finite-sized laser spot. The maxima take place below but near the surfaces because these are the zones that concentrate most of the embelin. The intensities decrease as the focusing point moves further within the sample; this is due to two causes: the embelin concentration decrement and the increment of the laser radiation absorption by the sample with depth. Although the important data dispersion —that can be attributed to the surface irregularity and porosity—, the location of the maxima is consistent with the results in Fig. 3; they indicate high embelin concentrations in a thin layer (about a few microns) below the surface. No systematic differences were found between the measurements for the top and bottom surfaces, thus embelin distributions can be considered symmetric with respect to the specimen mid-planes. The lack of symmetry observed in Fig. 3 is attributed to the lack of a well-defined sample edge that is difficult to access via lateral profiling.

4.4 Embelin release

Fig. 5 depicts the embelin released mass as function of time for specimens eE3 and eE6; error bars indicate the dispersion of the results. Release histories are divided into three stages: the burst stage (BS), which consists in the initial rapid release during approximately the first 12 h; a transition stage (TS) in which the mass release rate, $\frac{dm_{E_{rel}}}{dt}$, slows down; and the stable release state (SRS) which starts after approximately 48 h and lasts until embelin is completely exhausted (depletion times are approximately 400 h and 260 h for the eE3 and eE6, respectively). It is interesting to note that the times of the BS and the TS are roughly same for both specimens, although the difference in their embelin contents.

Weight checks showed that, consistently with its hydrophobic nature of PCL [29], the aqueous solution intakes were very low, around 0.5% the matrix weight during the first 10 h of immersion.

Embelin release rates during the BS and SRS can be assimilated to constants, as indicated

indicating 95% confidence bounds. Results in Table 1 show that release rate of eE6 is nearly 3 times that of eE3 during the BS, what is consistent with the larger amount of embelin eE6 releases during the first 12 h. Similarly, the release rate of eE6 during the SRS is approximately 2.4 times faster than that of eE3. This is not only because eE6 releases a larger amount of embelin during the SRS, but because it does it in a shorter time than eE3. When analyzed in terms of mass fraction, it is found that the eE3 releases approximately 41% of its embelin content during the BS and 59% during the SRS. On the other hand, the eE6 releases 52% and 48% of its embelin during the BS and the SRS, respectively.

A second set of in-depth Raman measurements was performed after 48 h of release (i.e., tests were interrupted approximately at the beginning of the SRS). The embelin intensity profiles are plot in Fig. 6. It is observed that the profiles have reduced their intensities with respect to those at the beginning of the test (Fig. 4), what it is consistent with the decrease in the embelin content. On the other hand, and in contrast to the measurements at the beginning of the test, the positions of the maxima are dispersed; they can be found up to about $20\,\mu m$ below the surface. These observations allow to infer that zones near the surfaces do not empty out of embelin during the initial stages, as is the usual assumption for burst models. The measurement at 48 h is in agreement with a significant part of the release during the burst is embelin from the bulk, while a significative portion of the embelin on or close the surface is released in the stable state.

4.5 Considerations about the experimental observations

The release rate of agent is influenced by characteristics of its dispersion and distribution in the matrix [30]. Thus, the development of the model starts from considerations about drug distribution in the film.

Raman measurements show initial embelin distributions that are compatible with that of casted films, in which the contraction experienced by the material during solvent evaporation results in the heterogeneous distribution of the solute. The embelin content across the thickness is intimate related to porosity. The simplest approach compatible with the observations in Section 4.2 is to assume that the film structure is not influenced by the embelin content, and so, the surface porosity is the same for eE3 and eE6. For the model, porosity profile is assumed piecewise constant; with a high porosity on the film surfaces, φ_l, consistent with the important embelin concentration in the surface layers, and a relatively low porosity in the film bulk, φ_b, which is ascribed to a fine porous microstructure with low embelin concentration.

A gross estimation of the mean film porosity can be calculated using the volume and weight of the eE3 and eE6 specimens and the density of the starting materials (Section 2). This results in a mean approximate porosity $\bar{\varphi} = 0.18$.

The constant rate of the drug delivery during SRS (Fig. 5) allows to infer that embelin

between the BS and SRS suggests the presence of two forms of embelin, which are assimilated to solid embelin and dissolved in PCL. Solid embelin is located on the film surface layer, where the porosity favors the formation of drug agglomerations [31]; dissolved embelin spreads across the complete film thickness highly dispersed.

Since aqueous solution penetration into the film is minimal due to the PCL hydrophobicity, wetting and subsequent embelin dissolution are limited to the porous zone close to the surfaces. The ingress of PBS into the surface layers triggers the dissolution of the embelin (agglomerated and dispersed) present in this zone. PCL is highly permeable to small drug molecules [32]; therefore, dispersed embelin could diffuse through the PCL amorphous domain until it dissolves in PBS when it reaches the wetted zone [23].

5 A mechanistic model of embelin release

5.1 Model formulation

Based on the above considerations, a model for the embelin release is proposed next. The model combines aqueous solution ingress and embelin diffusion and dissolution mechanisms. A model scheme is shown in Fig. 7. The problem is assumed one dimensional and symmetric with respect to the film mid-plane. The coordinate $z' = z - e/2$ is used as spatial reference, being e the film average thickness (Fig. 1e and 7a), such that the model domain spans $z' = [0,\ e/2]$.

Embelin is presented in the film in three forms: dispersed (embelin dispersed at the molecular level, and dissolved in the PCL amorphous domain), agglomerated (solid embelin), and dissolved in PBS. The hypothesis on the coexistence of these three forms of the solute is based on the work by Frenning [33], who observed this phenomenon in systems with high drug concentrations and/or when the drug is poorly soluble in aqueous solution. The mass concentrations of the three embelin forms, $C_{E_{dsp}}$, $C_{E_{agg}}$ and $C_{E_{dsv}}$, are given with respect to the film free volume,

$$dV(z') = (A\, dz') \cdot \varphi(z'), \tag{1}$$

where A is the specimen cross-section area and $\varphi(z')$ is the porosity. The overall embelin concentration is C_E=$C_{E_{dsp}} + C_{E_{agg}} + C_{E_{dsv}}$. The above concentrations evolve as function of the position, z', and time, t.

The embelin mass content at $t = 0$, m_E^0, is partitioned into dispersed, $m_{E_{dsp}}^0$, and agglomerated, $m_{E_{agg}}^0$, embelin, with partition coefficients given by

$$f_{E_{agg}}^0 = \frac{m_{E_{agg}}^0}{m_E^0} = \frac{2\int_0^{e/2} C_{E_{agg}}(z',0) \cdot \varphi(z') \cdot A dz'}{2\int_0^{e/2} C_E(z',0) \cdot \varphi(z') \cdot A dz'} \quad \text{and} \tag{2}$$

$$f_{E_{dsp}}^{0} = \frac{m_{E_{dsp}}^{0}}{m_{E}^{0}} = \frac{2\int_{0}^{e/2} C_{E_{dsp}}(z',0)\cdot\varphi(z')\cdot A\,dz'}{2\int_{0}^{e/2} C_{E}(z',0)\cdot\varphi(z')\cdot A\,dz'}, \tag{3}$$

with $f_{E_{dsp}}^{0} + f_{E_{agg}}^{0} = 1$.

The initial embelin concentration is

$$C_{E}(z',0) = C_{E_{dsp}}(z',0) + C_{E_{agg}}(z',0), \tag{4}$$

while the initial concentration of the dissolved embelin is zero,

$$C_{E_{dsv}}(z',0) = 0. \tag{5}$$

PBS ingress and diffusion into the film is governed by Fick's law [34],

$$\frac{\partial C_{Aq}(z',t)}{\partial t} = D_{Aq}\cdot\frac{\partial^{2} C_{Aq}(z',t)}{\partial z'^{2}}, \tag{6}$$

where C_{Aq} and D_{Aq} are the PBS concentration and diffusion coefficient, respectively. The initial PBS concentration is null inside the film

$$C_{Aq}(z',0) = 0, \tag{7}$$

and it is assumed to remain constant and equal to that of the solution bulk on the film surfaces

$$C_{Aq}(e/2\,,t) = C_{Aq_{bulk}}. \tag{8}$$

The symmetry condition at the PBS concentration at the film mid-plane is

$$\frac{dC_{Aq}(0,t)}{dz'} = 0. \tag{9}$$

Agglomerated embelin is impeded to diffuse until it dissolves. When reached by PBS (this is, for $C_{Aq} > 0$), the agglomerates dissolves following the Noyes-Whitney model [35] (Fig. 7b),

$$\frac{\partial C_{E_{agg}}}{\partial t} = -k_{E_{agg}} a_{E_{agg}} \langle C_{E_{sat}} - C_{E_{dsv}} \rangle \text{ if } C_{Aq} > 0 \text{ and } C_{E_{agg}} > 0, \tag{10}$$

where $k_{E_{agg}}$ is the dissolution coefficient, $a_{E_{agg}}$ is a coefficient that accounts for the area of the agglomerates exposed to PBS, and $C_{E_{sat}} = 0.13\,mg\cdot cm^{-3}$ is the embelin saturation limit in PBS [29]. The angle brackets $\langle\cdot\rangle$ adopt the value zero, and then no dissolution takes place, when $C_{E_{dsv}} \geq C_{E_{sat}}$, this is, when the embelin concentration attains the saturation limit. The condition $C_{E_{agg}} > 0$ prevents the model to dissolve more embelin than is

$$\frac{dC_{E_{agg}}(e/2\,,t)}{dz'} = 0; \tag{11}$$

the symmetry condition at the film mid-plane is

$$\frac{dC_{E_{agg}}(0,t)}{dz'} = 0. \tag{12}$$

Dispersed embelin diffusion is governed by Fick's law,

$$\frac{\partial C_{E_{dsp}}}{\partial t} = D_{E_{dsp}} \cdot \frac{\partial^2 C_{E_{dsp}}}{\partial z'^2} - k_{E_{dsp}} a_{E_{dsp}} \langle C_{E_{sat}} - C_{E_{dsv}} \rangle \quad \text{if} \;\; C_{Aq} > 0 \;\text{and}\; C_{E_{dsp}} > 0, \tag{13}$$

where $D_{E_{dsp}}$ and $k_{E_{dsp}}$ are the diffusion and the dissolution coefficients, respectively, and $a_{E_{dsp}}$ is a coefficient that accounts for the area exposed to PBS. The interpretation of the brackets $\langle\cdot\rangle$ and the condition $C_{E_{dsp}} > 0$ is the same as for the agglomerated embelin in Eq. (10).

As for the agglomerated form, it is assumed that dispersed embelin is not released into the PBS, so

$$\frac{dC_{E_{dsp}}(e/2\,,t)}{dz'} = 0; \tag{14}$$

the symmetry condition at the film mid-plane is

$$\frac{dC_{E_{dsp}}(0,t)}{dz'} = 0. \tag{15}$$

The mass balance for the dissolved embelin, $C_{E_{dsv}}$, is

$$\frac{\partial C_{E_{dsv}}}{\partial t} = D_{E_{dsv}} \frac{\partial^2 C_{E_{dsv}}}{\partial z'^2} + k_{E_{dsp}} a_{E_{dsp}} \langle C_{E_{sat}} - C_{E_{dsv}} \rangle + k_{E_{agg}} a_{E_{agg}} \langle C_{E_{sat}} - C_{E_{dsv}} \rangle \tag{16}$$

where $D_{E_{dsv}}$ is the diffusion coefficient. Dissolved embelin releases to the medium through the film surface. This external mass transport is characterized by the constant h and the driving force given by the difference between the embelin concentrations in the fluid bulk, $C_{E_{bulk}}$, and at the film surface, $C_{E_{dsv}}(e/2, t)$. Perfect sink condition is assumed throughout the experiment, meaning that the embelin concentration in the bulk fluid is negligible, $C_{E_{bulk}} \approx 0$ (less than 20% of the solubility value [12]). In this way, the boundary condition at the free surface is

$$\frac{dC_{E_{dsv}}(e/2, t)}{} \qquad h \qquad \qquad h$$

The boundary condition at the film mid-plane is given by the symmetry-condition,

$$\frac{dC_{E_{dsv}}(0,t)}{dz'} = 0. \tag{18}$$

The model assumes that the film matrix is inert and that it does not undergo neither degradation nor erosion during wetting and embelin release, as the hydrolytic degradation time of PCL is greater than the duration of the study [4]. Matrix swelling is neglected because its hydrophobicity.

5.2 Model implementation

In order to simplify the implementation and analysis, the model was rewritten in dimensionless form, with the dimensionless position and time given by $\zeta = \frac{z'}{(e/2)}$ (Fig. 7b) and $\tau = \frac{t \cdot D_{E_o}}{(e/2)^2}$, respectively. In this way, the dimensionless equations for the mass balance of PBS (Eq. 6) and for the agglomerated (Eq. 10), dispersed (Eq. 13) and dissolved embelin (Eq. 16) are:

$$\frac{\partial C'_{Aq}(\zeta,\tau)}{\partial \tau} = \frac{D_{Aq}}{D_{E_o}} \cdot \frac{\partial^2 C'_{Aq}(\zeta,\tau)}{\partial \zeta^2}\ , \tag{19}$$

$$\frac{\partial C'_{E_{agg}}(\zeta,\tau)}{\partial \tau} = -\frac{k_{E_{agg}} a_{E_{agg}} (e/2)^2}{D_{E_0}} \langle 1 - C'_{E_{dsv}} \rangle \text{ if } C'_{Aq} > 0 \text{ and } C'_{E_{agg}} > 0, \tag{20}$$

$$\frac{\partial C'_{E_{dsp}}(\zeta,\tau)}{\partial \tau} = \frac{D_{E_{dsp}}}{D_{E_0}} \cdot \frac{\partial^2 C'_{E_{dsp}}}{\partial \zeta^2} - \frac{k_{E_{dsp}} a_{E_{dsp}} (e/2)^2}{D_{E_0}} \langle 1 - C'_{E_{dsv}} \rangle \quad \text{if } C'_{Aq} > 0 \text{ and } C'_{E_{dsp}} > 0, \tag{21}$$

and

$$\frac{\partial C'_{E_{dsv}}(\zeta,\tau)}{\partial \tau} = \frac{D_{E_{dsv}}}{D_{E_0}} \frac{\partial^2 C'_{E_{dsv}}}{\partial \zeta^2} + \frac{k_{E_{dsp}} a_{E_{dsp}} (e/2)^2}{D_{E_0}} \langle 1 - C'_{E_{dsv}} \rangle + \frac{k_{E_{agg}} a_{E_{agg}} (e/2)^2}{D_{E_0}} \langle 1 - C'_{E_{dsv}} \rangle, \tag{22}$$

where the dimensionless concentrations are $C'_{Aq} = \frac{C_{Aq}}{C_{Aq_{bulk}}}$, $C'_{E_{agg}} = \frac{C_{E_{agg}}}{C_{E_{sat}}}$, $C'_{E_{dsp}} = \frac{C_{E_{dsp}}}{C_{E_{sat}}}$ and $C'_{E_{dsv}} = \frac{C_{E_{dsv}}}{C_{E_{sat}}}$; D_{E_0} is the diffusivity of embelin in the liquid-filled pores of the PCL matrix.

$$C'_{Aq}(1,\tau) = C_{Aq_{bulk}}/C_{Aq_{bulk}} = 1 \quad \text{and} \quad \frac{dC'_{Aq}(0,\tau)}{d\zeta} = 0\,; \tag{23}$$

those of the agglomerated embelin (Eq. 11 and 12) are

$$\frac{dC'_{E_{agg}}(1,\tau)}{d\zeta} = \frac{dC'_{E_{agg}}(0,\tau)}{d\zeta} = 0\,; \tag{24}$$

those of the dispersed embelin (Eqs. 14 and 15) are

$$\frac{dC'_{E_{dsp}}(1,\tau)}{d\zeta} = \frac{dC'_{E_{dsp}}(0,\tau)}{d\zeta} = 0\,; \tag{25}$$

and those of the dissolved embelin (Eqs. 17 and 18) are

$$\frac{dC'_{E_{dsv}}(1,\tau)}{d\zeta} = -\frac{h\cdot(e/2)}{D_{E_o}}C'_{E_{dsv}} \quad \text{and} \quad \frac{dC'_{E_{dsv}}(0,\tau)}{d\zeta} = 0. \tag{26}$$

The model was implemented in MATLAB with PDEPE for the solution of one-dimensional parabolic and elliptic partial differential equations by means of a finite difference scheme. The model domain, $\zeta = [0,1]$, was discretized with 900 elements, 90% of which were concentrated in the zone next to the film surface, $\zeta = [0.9,1]$.

5.3 Model tuning

The model requires the tuning of the following data and parameters: the initial spatial embelin distribution and its partition into the dispersed and agglomerated forms; the PBS diffusion coefficient, D_{Aq}; the diffusion coefficients of the dispersed, agglomerated and dissolved embelin in the PCL matrix, $D_{E_{dsp}}$, $D_{E_{agg}}$ and $D_{E_{dsv}}$, the diffusion coefficient of embelin in the fluid-filled pores, D_{E_o}; the dissolution coefficients of the dispersed and agglomerated embelin, $k_{E_{dsp}}$ and $k_{E_{agg}}$; the coefficients that account for the area of the dispersed and agglomerated embelin that is exposed to PBS during the dissolution, $a_{E_{dsp}}$ and $a_{E_{agg}}$; the coefficient of the external mass transport, h; and the porosity profile across the film thickness, $\varphi(z')$.

The above data and parameters are tuned so that the model embelin release matches those of the experiments in Fig. 5. In this way, the model tuning is formulated as an optimization problem, the objective function of which is the minimization of the sum of the normalized square differences between the model and experimental embelin release histories:

$$R = \min_{P} \frac{1}{n} \sum_{i=1}^{n} \left[\frac{m_{E_{rel}}(t_i) - \overline{m_{E_{rel}}^{exp}}(t_i)}{m_E^0} \right]^2, \tag{27}$$

where P is the set of the model parameters, $m_{E_{rel}}(t_i)$ is the model prediction for the accumulated embelin release up to time t_i, which is computed by doing

$$m_{E_{rel}}(t_i) = m_E^0 - \int_0^{t_i} 2 \int_0^{e/2} C_E(z', t) \cdot \varphi(z') \cdot A dz' \, dt \, ; \tag{28}$$

and $\overline{m_{E_{rel}}^{exp}}(t_i)$ are the experimental data points in Fig. 5. The explicit form for the vector of the optimization variables P is given at the end of this section once all the considerations for the analysis are presented.

The optimization is carried out under the following restrictions and considerations:

a. The embelin spatial distribution in time should evolve compatible with the Raman measurements in Figs. 3, 4 and 6. The initial spatial concentrations of the agglomerated and dispersed embelin were modelled using the following inverse exponential functions

$$C'_{E_{agg}}(\zeta, 0) = \frac{\alpha_{E_{agg}}^0}{1 + e^{-\beta_{E_{agg}}^0 (\zeta - \zeta_l)}} \quad \text{and} \tag{29}$$

$$C'_{E_{dsp}}(\zeta, 0) = \frac{\alpha_{E_{dsp}}^0}{1 + e^{-\beta_{E_{dsp}}^0 (\zeta - 1)}} \tag{30}$$

with the constants the $\alpha_{E_{agg}}^0$, $\alpha_{E_{dsp}}^0$, $\beta_{E_{agg}}^0$ and $\beta_{E_{dsp}}^0$ tuned such that $C'_{E_{agg}}(\zeta, 0)$ and $C'_{E_{dsp}}(\zeta, 0)$ correspond to the agglomerated and dispersed embelin partitions in Eq. (2) and (3), respectively. The surface layer thickness, ζ_l, is expected to be of a few microns, of the same order of the experimental measurements of the surface pore size.

Besides, the resulting initial embelin distribution

$$C'_E(\zeta, 0) = C'_{E_{agg}}(\zeta, 0) + C'_{E_{dsp}}(\zeta, 0) \tag{31}$$

should be compatible with the Raman intensity profiles at $t = 0$.

Based on the model considerations (Section 4.5) the porosity profile is assumed φ_b for the film bulk and φ_l for the surface layer. In this way, the initial embelin mass content can be expressed in terms of the concentrations in Eqs. (29) and (30) via (31) as follows

$$m_E^0 = 2 C_{E_{sat}} A \frac{e}{2} \left[\int_0^{\zeta_l} C'_E(\zeta, 0) \varphi_b d\zeta \; + \int_{\zeta_l}^{1} C'_E(\zeta, 0) \varphi_l d\zeta \right], \tag{32}$$

where the values for $\alpha_{E_{agg}}^0$, $\alpha_{E_{dsp}}^0$, $\beta_{E_{agg}}^0$, $\beta_{E_{dsp}}^0$ and ζ_l are left open to be tuned

Diffusion coefficients are assumed independent of concentrations. This assumption, while not conceptually correct, has been largely applied due to the computational simplicity [23].

- Preliminary qualitative parametric studies showed that D_{Aq} is the critical parameter for the model tuning. No data on PBS diffusion in casted PCL films was found in the literature. The only data found was for the diffusion of water in a casted PCL film reported by Peng et al. [36]. Peng et al. used infrared correlation spectroscopy to estimate a diffusion coefficient of $3.3 \cdot 10^{-6}\ cm^2\ h^{-1}$ at 26 °C. Unfortunately, Peng et al. do not report the film porosity. It has to be also noted that diffusion coefficient in polymers strongly depends on temperature [37]. The above issues do not allow to assimilate Peng's diffusion coefficient to D_{Aq}, but they show that temperature could be a critical parameter. On the other hand, D_{Aq} must be compatible with PBS intake, which was measured lower than 0.5 wt% after 10 h.
- Data from the bibliography show that effective diffusion coefficients of drugs in PBS-filled pores in films and other matrix geometries are of magnitude less than $10^{-3}\ cm^2 h^{-1}$ [11,32,38–42]. This range is used as reference for D_{E_o} in our work.
- The diffusion coefficient of the dissolved embelin is assumed equal the diffusion coefficient of the embelin in PBS-filled pores, so $D_{E_{dsv}} = D_{E_o}$.
- Based on the work of Grassi et al. [41], the diffusion coefficient of the dispersed embelin in the matrix is assumed an order of magnitude less than the diffusion in the PBS-filled pores, this is $D_{E_{dsp}} = 0.1 D_{E_o}$.
- Since embelin agglomerates cannot diffuse, its diffusion coefficient is set $D_{E_{agg}} = 0$.

b. The dissolution and area coefficients for the dispersed and agglomerated embelin were grouped in $k'_{E_{dsp}} = k_{E_{dsp}} a_{E_{dsp}}$ and $k'_{E_{agg}} = k_{E_{agg}} a_{E_{agg}}$ and handled as single parameters. Following the studies of Chang et al. [43], they are treated as adjustable parameters.

c. Preliminary qualitative parametric studies showed that the effect of the resistance to the external mass transport is negligible when the perfect sink condition is assumed. Consequently, the external transport coefficient is set with a remarkably high value, say $h = 1000\ cm^{-1}$.

Based on the above considerations, the explicit form for the vector of the optimization variables is

$$P = \left[\alpha^0_{E_{agg}}, \beta^0_{E_{agg}}, \alpha^0_{E_{dsp}}, \beta^0_{E_{dsp}}, \varphi_l, \zeta_l, D_{Aq}, D_{E_o}, k'_{E_{dsp}}, k'_{E_{agg}}\right]. \quad (33)$$

5.4 Model application and analysis

implementation of optimization algorithms unfruitful. Thus, the values for the design variables (Eq. 33) that result in the best fit of the objective function (Eq. 27) for the embelin release experiments were found by trial and error, using a procedure that attended to the constraints and considerations discussed in Section 5.3.

Embelin release histories of the optimized models are depicted in Fig. 8 along with the experimental data. Note that in contrast to the experimental results in Fig. 5, embelin releases are now plotted as fractions of the initial embelin content, $\frac{m_{E_{rel}}}{m_E^0}$, such that the limit value $\frac{m_{E_{rel}}}{m_E^0} = 1$ indicates that embelin contents are completely depleted. Residuals of the objective function (Eq. 27) are $R = 9 \cdot 10^{-4}$ and $18 \cdot 10^{-4}$ for eE3 and eE6, respectively. The mean relative deviations of the model from the experimental data are 3 and 4%. Maximum deviations of the model predictions from the experimental data are found in the beginning of the test (during the first hours of immersion) and during the transition from the BS to the TS, where the model overestimates the experimental values.

The initial embelin concentration $C_E'(z)$ profiles are shown in Fig. 9. The associated values for the variables $\alpha_{E_{agg}}^0, \beta_{E_{agg}}^0, \alpha_{E_{dsp}}^0, \beta_{E_{dsp}}^0$, φ_l, φ_b and ζ_l are reported in Table 2 along with the resulting overall partition coefficients for the agglomerated embelin, $f_{E_{agg}}^0$. The values of $f_{E_{agg}}^0$ indicate that eE6 contains a lower proportion of agglomerated embelin than eE3, that could be related with the high amount of excess embelin that is exuded in solid form during the film preparation. The surface layer contains approximately 63% of the initial embelin load of eE3, being 78% of the embelin in the surface layer in the agglomerated form. For eE6, the surface layer contains approximately 53% of the initial embelin load, with 67% of the embelin in the surface layer being in the agglomerated form. These high embelin concentrations on the surfaces are compatible with the Raman results in Section 4.3, Fig. 10.

The boundary layer extents are set to $12.3\ \mu m$ for both specimens (shaded areas in Fig. 9), the same order of the surface porosity size (Section 4.2). Porosity of the surface layers is $\varphi_l = 0.9$, compatible with the observations in Section 4.2. Mean bulk porosity is set $\varphi_b = 0.15$ in order to attain the mean porosity value $\bar{\varphi}$ (Section 4.5).

The proposed initial embelin distributions were checked for compatibility with Raman intensity measurements. To carried out proper comparisons, model predictions were convoluted with the instrumental response (Section 3.3). The results are plotted in Fig. 10, where the shaded areas are the envelopes of the experimental intensity profiles in Fig. 4. It is worth noting that these comparisons are qualitative, as the numerical results are scaled to make them compatible with the experimental data. Despite the scaling, it is interesting to see that both sets of results have their maxima a few microns below the surface.

this coefficient, $5 \cdot 10^{-10}\, cm^2\, h^{-1} \lesssim D_{Aq} \lesssim 2 \cdot 10^{-9}\, cm^2\, h^{-1}$, that allows for dissolution-controlled models. Additionally, this range for the D_{Aq} satisfies experimental PBS intake constrain (less than 0.5 wt% after 10 h of immersion). PBS diffusion coefficients lower than $5 \cdot 10^{-10}\, cm^2\, h^{-1}$ do not allow the intake of the amount of fluid necessary for the embelin dissolution and its complete release. The best fits between experimental and numerical results were for $D_{Aq} = 1 \cdot 10^{-9}\, cm^2\, h^{-1}$.

The effective diffusion coefficients of embelin in PBS-filled pores was set $D_{E_o} = 0.0008\, cm^2 \cdot h^{-1}$, what is compatible with the considerations made in Section 5.3. In the same way as with the D_{Aq}, the D_{E_o} was set the same for the two samples.

In contrast to the diffusion coefficients above, no unique value for the dissolution coefficients $k'_{E_{dsp}}$ and $k'_{E_{agg}}$ could be used for both samples. Dissolution coefficients are $k'^{E2.9s}_{E_{dsp}} = 3200\, h^{-1}$ and $k'^{E2.9s}_{E_{agg}} = 9.8\, h^{-1}$ for eE3, and $k'^{E6.1s}_{E_{dsp}} = 11600\, h^{-1}$ and $k'^{E6.1s}_{E_{agg}} = 23.5\, h^{-1}$ for eE6. Consistent with the higher release rates of eE6 during the BS and SRS (Table 1), dissolution coefficients of eE6 are both higher than those of eE3. This behavior is attributed to the larger exposed area of agglomerates to PBS for eE6, which are mainly concentrated in the surface layer, thus favoring the release. Furthermore, the dissolution coefficients of the agglomerated embelin are lower than those of the dispersed ones; this reflects the smaller exposed area per unit mass of the agglomerated embelin with respect to the dispersed one.

The results for the time evolution of the normalized embelin concentration are plot in Fig. 9. Results for $t \leq 48\, h$ (or in other words, for BS and TS) show a small but extended reduction in the embelin concentration; this behavior is clearer for eE6, for which the reduction in the embelin concentration beyond the boundary layer is evident. Besides, for $t > 48\, h$ (this is, for the SRS) the embelin concentration reduction occurs in the boundary layer. It is interesting to observe that the embelin profiles present transition points during the SRS (marked with circles in Fig. 9), which are associated with dissolution of the agglomerated embelin. Note that transition points move deeper into the sample during the early SRS (see the evolutions from $t = 48\, h$ to $t = 100\, h$ and $t = 150\, h$ of eE3 and eE6, respectively), following the PBS penetration and the embelin dissolution. Then, once the agglomerated embelin located beyond the boundary layer is depleted, the transition points move towards the sample surface (see the profile for $t = 200\, h$ and $t = 300\, h$ of eE3 and eE6, respectively).

Fig. 11 compares the Raman experimental measurements in Fig. 6 with the simulated intensity profiles of the numerical predictions for $t = 48\, h$. It is observed that both sets of results are compatible with the presence of embelin in the zone next to the surface, which we associate to the agglomerated embelin. Fig. 11a shows that experimental profile and

experimental measurements move deeper into the sample (about $10\ \mu m$ to $15\ \mu m$), while the peak of the model results remains in the same position next to the surface (Fig. 11b). As it was already discussed when dealing with the dispersion in the Raman intensity measurements in Section 4.3, the deep location of the peak of eE6 is attributed to the porosity on the specimen surface. It is argued that, as embelin is released from the pores, there is more uncertainty in the detection of the specimen surface, which is systematically detected towards the interior of the specimen. We support this hypothesis on the fact that there is no means by which embelin can penetrate deeper into the sample.

The criterion proposed by Chang and Himmelstein [43] is used to assess whether diffusion or dissolution preponderates in the kinetics of the different mechanisms in the model. This criterion states that dissolution is the rate-limiting mechanism when $\left(\frac{D_E}{L^2}\right)^{-1} \ll {k'_E}^{-1}$ (and vice-versa), where L is characteristic diffusion length in the range $0 < L < e/2$. Table 3 summarizes the resistance coefficients for the diffusion of PBS, dispersed and dissolved embelin, and for the dissolution of dispersed and agglomerated embelin. Note that the characteristic length has been set equal to surface layer for PBS and dissolved embelin, since these two species diffuse the distance of the surface layer extent $\left((e/2)\cdot(1-\zeta_l)\right)$; in contrast, the characteristic length for the dissolved embelin has been set equal to $e/2$, since this specie diffuses from the interior of the specimen to the free surface. It is observed from Table 3 that the maximum resistance is for PBS diffusion, so PBS ingress dominates embelin dissolution rates and dissolved embelin diffusion. Dissolution coefficients of the dispersed embelin present the lowest resistances and they are dominated by dispersed embelin diffusion resistance (which does not need of the PBS ingress). Dissolution of agglomerated embelin and diffusion of dissolved embelin have comparable resistances. The above observations show that besides the high resistance to PBS ingress, the dominant embelin release mechanisms are: the diffusion of the dispersed embelin during the BS and the dissolution of the agglomerated embelin during SRS.

The conclusions in the previous paragraph are corroborated by the plots in Fig. 12, which illustrate the model predictions for the release histories of the agglomerated and dispersed embelin. Released embelin masses are normalized with respect to their initial contents, such that $\frac{m_{E_{agg}}}{m^0_{E_{agg}}} = 1$ and $\frac{m_{E_{dsp}}}{m^0_{E_{dsp}}} = 1$ indicate that agglomerated and dissolved embelin contents are depleted, respectively. It can be observed from the plots that embelin release during the BS consists mainly of dispersed embelin, which decelerates during the TS and until it extinguishes before by the end of the TS. On the other hand, the release of agglomerated embelin is negligible during the BS (mainly in eE3), it accelerates during the TS and keeps a nearly constant rate during the SRS until depletion.

6 Conclusions

based on the results of embelin release experiments and optical and confocal Raman microscopy observations. The model assumes a dual dispersion of the embelin: agglomerated and dispersed. Agglomerated embelin is initially located in boundary layer next to the surfaces, while dispersed embelin spreads throughout the film. Embelin release mechanism combines the effects of the aqueous solution migration into the film, the embelin diffusion and the embelin dissolution when in contact with the aqueous solution. Diffusion coefficient for the liquid ingress into the film is the critical parameter for the model tuning. The dominant embelin release mechanisms are the diffusion of the dispersed embelin during the burst stage, and the dissolution of the agglomerated embelin during stable release stage.

Although developed for the embelin-PCL system, the proposed mechanistic model could be applied to tune for other poorly soluble drugs provided that the matrix is inert, this is, it does not undergo neither degradation, erosion nor swelling during wetting and drug release. The model is flexible in what respects to the initial distribution of the drug forms. Furthermore, the model could be extended to incorporate concentration-dependent dissolution coefficients in order to account for the reduction of the agglomerates size (and consequently, the exposed area) as the dissolution progresses.

7 Acknowledgments

This work has been supported by the National Scientific and Technical Research Council of Argentina (grants PUE073 and PIP 2017/001), the Argentinian Agency for Scientific and Technological Promotion (grant PICT 2017/1607) and the Nacional University of Mar del Plata (grant ING516/18). The authors thank the Biotechnology Institute of the Faculty of Engineering of the National University of San Juan for providing the embelin used in this work.

8 Data Availability

The raw/processed data required to reproduce these findings cannot be shared at this time as the data also forms part of an ongoing study.

9 List of symbols

A	Specimen cross-section area.
$a_{E_{agg}}$	Coefficient to account for the area of the agglomerates exposed to PBS.
$a_{E_{dsp}}$	Coefficient to account for the area of the dispersed embelin exposed to PBS.
d	Specimen diameter.
e	Specimen thickness.
C_E	Overall embelin mass concentration.
$C_{E_{bulk}}$	Embelin concentration in the fluid bulk.

$C_{E_{agg}}$	Agglomerated embelin mass concentration.
$C_{E_{dsv}}$	Dissolved embelin mass concentration.
$C_{E_{sat}}$	Embelin saturation limit in PBS.
C_{Aq}	PBS mass concentration.
$C_{Aq_{bulk}}$	PBS mass concentration at the fluid bulk.
C'_{E}	Dimensionless overall embelin mass concentration.
$C'_{E_{dsp}}$	Dimensionless dispersed embelin mass concentration.
$C'_{E_{agg}}$	Dimensionless agglomerated embelin mass concentration.
$C'_{E_{dsv}}$	Dimensionless dissolved embelin mass concentration.
C'_{Aq}	Dimensionless PBS mass concentration.
D_{E_0}	Embelin diffusion coefficient in the fluid-filled pores.
D_{Aq}	PBS diffusion coefficient.
$f^0_{E_{agg}}$	Partition coefficient of the initial agglomerated embelin mass content.
$f^0_{E_{dsp}}$	Partition coefficient of the initial dispersed embelin mass content.
h	External transport coefficient.
$k_{E_{agg}}$	Agglomerated embelin dissolution coefficient.
$k_{E_{dsp}}$	Dispersed embelin dissolution coefficient.
m^0_E	Initial overall embelin mass content.
$m^0_{E_{agg}}$	Initial agglomerated embelin mass content.
$m^0_{E_{dsp}}$	Initial dispersed embelin mass content.
$m_{E_{rel}}$	Embelin released mass.
$m^{exp}_{E_{rel}}$	Experimental results for the embelin released mass.
P	Model parameter set.
t	Time.
z	Through-the-thickness position with origin at the specimen surface.
z'	Through-the-thickness position with origin at the specimen mid-plane.
z'_l	Surface layer extent.
$\alpha^0_{E_{agg}}, \beta^0_{E_{agg}}$	Fitting coefficients for the initial $C'_{E_{agg}}$.
$\alpha^0_{E_{dsp}}, \beta^0_{E_{dsp}}$	Fitting coefficients for the initial $C'_{E_{dsp}}$.
φ	Porosity as function of the position.
$\bar{\varphi}$	Specimen mean porosity.
φ_b	Bulk porosity.
φ_l	Surface layer porosity.
ζ	Dimensionless through-the-thickness position with origin at the specimen mid-plane.
ζ_l	Dimensionless surface layer extent.
τ	Dimensionless time.

[1] E. Schlesinger, N. Ciaccio, T.A. Desai, Polycaprolactone thin- fi lm drug delivery systems : Empirical and predictive models for device design, Mater. Sci. Eng. C. 57 (2015) 232–239. doi:10.1016/j.msec.2015.07.027.

[2] S. Senapati, A.K. Mahanta, S. Kumar, P. Maiti, Controlled drug delivery vehicles for cancer treatment and their performance, Signal Transduct. Target. Ther. 3 (2018) 1–19. doi:10.1038/s41392-017-0004-3.

[3] J.G. Fernandes, D.M. Correia, G. Botelho, J. Padrão, F. Dourado, C. Ribeiro, S. Lanceros-Méndez, V. Sencadas, PHB-PEO electrospun fiber membranes containing chlorhexidine for drug delivery applications, Polym. Test. 34 (2014) 64–71. doi:10.1016/j.polymertesting.2013.12.007.

[4] T.K. Dash, V.B. Konkimalla, Poly-ϵ-caprolactone based formulations for drug delivery and tissue engineering: A review, J. Control. Release. 158 (2012) 15–33. doi:10.1016/j.jconrel.2011.09.064.

[5] R. Poojari, Embelin-a drug of antiquity: Shifting the paradigm towards modern medicine, Expert Opin. Investig. Drugs. 23 (2014) 427–444. doi:10.1517/13543784.2014.867016.

[6] D.R. Swami, N.P. Malpathak, Exploring in-vivo and in-vitro Oxalis Corniculata L. for phytochemicals using non-targeted LC-MS approach and its antioxidant capacity, Int. J. Pharm. Sci. Res. 9 (2018) 4151–4157. doi:10.13040/IJPSR.0975-8232.9(10).4151-57.

[7] C. Sivasankar, S. Gayathri, J.P. Bhaskar, V. Krishnan, S.K. Pandian, Evaluation of selected Indian medicinal plants for antagonistic potential against Malassezia spp. and the synergistic effect of embelin in combination with ketoconazole, Microb. Pathog. 110 (2017) 66–72. doi:10.1016/j.micpath.2017.06.026.

[8] P.R. Cortez Tornello, G.E. Feresin, A. Tapia, M. Dzieciuch, T.R. Cuadrado, G.A. Abraham, Effect of processing techniques on new poly(ε-caprolactone)-embelin microparticles of biomedical interest, Adv. Polym. Technol. (2017) 1–11. doi:10.1002/adv.21814.

[9] P.R. Cortez Tornello, G.E. Feresin, A. Tapia, T.R. Cuadrado, G.A. Abraham, Multilayered electrospun nanofibrous scaffolds for tailored controlled release of embelin, Soft Mater. 16 (2018) 51–61. doi:10.1080/1539445X.2017.1398173.

[10] E. Luong-Van, L. Grøndahl, K.N. Chua, K.W. Leong, V. Nurcombe, S.M. Cool, Controlled release of heparin from poly(e-caprolactone) electrospun fibers, Biomaterials. 27 (2006) 2042–2050. doi:10.1016/j.biomaterials.2005.10.028.

[11] L.L. Lao, S.S. Venkatraman, N.A. Peppas, Modeling of drug release from biodegradable polymer blends, Eur. J. Pharm. Biopharm. 70 (2008) 796–803. doi:10.1016/j.ejpb.2008.05.024.

[12] P.R. Cortez Tornello, G.E. Feresin, A. Tapia, I.G. Veiga, Â.M. Moraes, G.A. Abraham, T.R. Cuadrado, Dispersion and release of embelin from electrospun, biodegradable, polymeric membranes, Polym. J. 44 (2012) 1105–1111. doi:10.1038/pj.2012.80.

[13] P.R. Cortez Tornello, P.C. Caracciolo, T.R. Cuadrado, G.A. Abraham, Structural characterization of electrospun micro/nanofibrous scaffolds by liquid extrusion porosimetry: A comparison with other techniques, Mater. Sci. Eng. C. 41 (2014) 335–342. doi:10.1016/j.msec.2014.04.065.

electrohydrodynamic atomization (CEHDA) technique, J. Mater. Chem. B. 3 (2015) 102–111. doi:10.1039/C4TB00664J.

[15] J. Siepmann, R.A. Siegel, M.J. Rathbone, Fundamentals and applications of controlled release drug delivery, Springer, New York, 2012. doi:10.1007/978-1-4614-0881-9.

[16] V. Bugatti, M.R. Acocella, M. Maggio, G. Vigliotta, R. Pantani, G. Gorrasi, Effect of Draw Ratio on Physical, Release, and Antibacterial Properties of Poly(ε-caprolactone) Loaded with Lysozyme, Macromol. Mater. Eng. 302 (2017) 1–9. doi:10.1002/mame.201700367.

[17] J. Siepmann, F. Siepmann, Mathematical modeling of drug delivery, Int. J. Pharm. 364 (2008) 328–343. doi:10.1016/j.ijpharm.2008.09.004.

[18] J. Siepmann, F. Siepmann, Modeling of diffusion controlled drug delivery, J. Control. Release. 161 (2012) 351–362. doi:10.1016/j.jconrel.2011.10.006.

[19] E.M. Ouriemchi, T.P. Ghosh, J.M. Vergnaud, Transdermal drug transfer from a polymer device: Study of the polymer and the process, Polym. Test. 19 (2000) 889–897. doi:10.1016/S0142-9418(99)00059-8.

[20] J. Siepmann, N.A. Peppas, Modeling of drug release from delivery systems based on hydroxypropyl methylcellulose (HPMC), Adv. Drug Deliv. Rev. 48 (2001) 139–157. doi:10.1016/S0169-409X(01)00112-0.

[21] G. Frenning, Modelling drug release from inert matrix systems: From moving-boundary to continuous-field descriptions, Int. J. Pharm. 418 (2011) 88–99. doi:10.1016/j.ijpharm.2010.11.030.

[22] T. Higuchi, Rate of release of medicaments from ointment bases containing drugs in suspension., J. Pharm. Sci. 50 (1961) 874–875. doi:10.1248/cpb.23.3288.

[23] J. Siepmann, N.A. Peppas, Higuchi equation: Derivation, applications, use and misuse, Int. J. Pharm. 418 (2011) 6–12. doi:10.1016/j.ijpharm.2011.03.051.

[24] G.E. Feresin, A. Tapia, M. Sortino, S. Zacchino, A.R. de Arias, A. Inchausti, G. Yaluff, J. Rodriguez, C. Theoduloz, G. Schmeda-Hirschmann, Bioactive alkyl phenols and embelin from Oxalis erythrorhiza., J. Ethnopharmacol. 88 (2003) 241–7. http://www.ncbi.nlm.nih.gov/pubmed/12963150 (accessed August 23, 2018).

[25] S.B. Prasad, M. Bist, S.P. Verma, Development and validation of the UV-spectrophotometric method for determination of embelin, Int. J. Pharm. Qual. Assur. 7 (2016) 51–54. doi:10.25258/ijpqa.7.3.4.

[26] J.P. Tomba, E.D. La Puente, J.M. Pastor, Calculation of polymer blend compositions from Raman spectra: A new method based on parameter estimation techniques, J. Polym. Sci. Part B Polym. Phys. 38 (2000) 1013–1023. doi:10.1002/(SICI)1099-0488(20000415)38:8<1013::AID-POLB2>3.0.CO;2-6.

[27] N. Everall, The influence of out-of-focus sample regions on the surface specificity of confocal Raman microscopy, Appl. Spectrosc. 62 (2008) 591–598. doi:10.1366/000370208784658057.

[28] J.P. Tomba, M. de la Paz Miguel, C.J. Perez, Correction of optical distortions in dry depth profiling with confocal Raman microspectroscopy, J. Raman Spectrosc. 42 (2011) 1330–1334. doi:10.1002/jrs.2843.

[29] P.R. Cortez Tornello, Sistemas poliméricos biocompatibles para liberación controlada de Embelina, Universidad Nacional de Mar del Plata, 2015.

[31] G.A. Abraham, T.R. Cuadrado, Modeling of Segmented Polyurethane Drying Process, Int. Polym. Process. 13 (1998) 369–378. doi:10.3139/217.980369.
[32] C.G. Pitt, A.R. Jeffcoat, R.A. Zweidinger, A. Schindler, Sustained Drug Delivery Systems. I. The Permeability of Poly(e-Caprolactone), Poly(DL - Lactic Acid), and Their Copolymers, J. Biomed. Mater. Res. 13 (1979) 497–507.
[33] G. Frenning, Theoretical investigation of drug release from planar matrix systems: Effects of a finite dissolution rate, J. Control. Release. 92 (2003) 331–339. doi:10.1016/S0168-3659(03)00338-9.
[34] P.Y. Le Gac, D. Choqueuse, D. Melot, Description and modeling of polyurethane hydrolysis used as thermal insulation in oil offshore conditions, Polym. Test. 32 (2013) 1588–1593. doi:10.1016/j.polymertesting.2013.10.009.
[35] S. McGinty, G. Pontrelli, A general model of coupled drug release and tissue absorption for drug delivery devices, J. Control. Release. 217 (2015) 327–336. doi:10.1016/j.jconrel.2015.09.025.
[36] Y. Peng, P. Wu, Y. Yang, Two-dimensional infrared correlation spectroscopy as a probe of sequential events in the diffusion process of water in poly(ε-caprolactone), J. Chem. Phys. 119 (2003) 8075–8079. doi:10.1063/1.1610441.
[37] C. Yang, X. Xing, Z. Li, S. Zhang, A comprehensive review on water diffusion in polymers focusing on the polymer-metal interface combination, Polymers (Basel). 12 (2020). doi:10.3390/polym12010137.
[38] F. Wang, G.M. Saidel, J. Gao, A mechanistic model of controlled drug release from polymer millirods: Effects of excipients and complex binding, J. Control. Release. 119 (2007) 111–120. doi:10.1016/j.jconrel.2007.01.019.
[39] K. Sevim, J. Pan, A Mechanistic Model for Acidic Drug Release Using Microspheres Made of PLGA 50:50, Mol. Pharm. 13 (2016) 2729–2735. doi:10.1021/acs.molpharmaceut.6b00313.
[40] S.Y. Lee, B.R. Lee, J. Lee, S. Kim, J.K. Kim, Y.H. Jeong, S. Jin, Microscale diffusion measurements and simulation of a scaffold with a permeable strut, Int. J. Mol. Sci. 14 (2013) 20157–20170. doi:10.3390/ijms141020157.
[41] M. Grassi, D. Voinovich, E. Franceschinis, B. Perissutti, J. Filipovic-Grcic, Theoretical and experimental study on theophylline release from stearic acid cylindrical delivery systems, J. Control. Release. 92 (2003) 275–289. doi:10.1016/S0168-3659(03)00330-4.
[42] D.J. Maxwell, B.C. Hicks, S. Parsons, S.E. Sakiyama-Elbert, Development of rationally designed affinity-based drug delivery systems, Acta Biomater. 1 (2005) 101–113. doi:10.1016/j.actbio.2004.09.002.
[43] N.J. Chang, K.J. Himmelstein, Dissolution-diffusion controlled constant-rate release from heterogeneously loaded drug-containing materials, J. Control. Release. 12 (1990) 201–212. doi:10.1016/0168-3659(90)90101-X.

Captions to the figures

Figure 1: Sample preparation and testing: (a) PCL structure, (b) embelin structure, (c) schematic of the specimen obtention from the films, (d) specimen for Raman analysis and (e) schematic of the delivery test.

Figure 2: SEM micrograph of the surface of a E3 sample.

Figure 3: (a) Raman spectra of embelin, PCL and an embelin loaded PCL sample. (b) Initial embelin intensity across the thickness for specimen eE6.

Figure 4. Initial embelin intensity profiles in the zones next to the specimen surfaces.

Figure 5. Embelin released mass as function of time for eE3 and eE6 specimens.

Figure 6. Embelin intensity profiles in the zone next to the specimen surfaces after 48 h of release.

Figure 7. Scheme of the embelin release model: (a) Initial embelin distribution, dispersed embelin diffusion and water ingress; (b) Embelin dissolution, diffusion and release.

Figure 8. Model predictions of the embelin release histories and comparisons with the experimental data.

Figure 9. Time evolution of the embelin spatial distribution for specimens (a) eE3 and (b) eE6. Circles indicate the transition points and shaded areas represent the surface layer extent.

Figure 10. Initial embelin distribution: comparison between the simulated Raman intensity profiles and the experimental measurement for specimens (a) eE3 and (b) eE6.

Figure 11: Spatial embelin distribution after 48 h: comparison between the convoluted model results and the experimental measurements (a) eE3 and (b) eE6.

Figure 12: Model predictions for dispersed and agglomerated embelin release of samples (a) eE3 and (b) eE6. Agglomerated and dispersed masses are normalized with respect to the initial contents $m^0_{E_{dsp}}$ and $m^0_{E_{agg}}$, respectively.

Tables

Table 1. Estimations of the embelin release rates at the burst and stable release stages.

	Embelin release rate $[mg/h]$	
	eE3	eE6
Burst stage (BS)	0.0660 ± 0.0075	0.1823 ± 0.0179
Stable release stage (SRS)	$0.0022 \pm 1{\cdot}10^{-4}$	$0.0052 \pm 4{\cdot}10^{-4}$

Table 2. Values of the parameters that define and characterize the initial spatial embelin distribution.

Analysis case	$\alpha^0_{E_{agg}}$	$\beta^0_{E_{agg}}$	$\alpha^0_{E_{dsp}}$	$\beta^0_{E_{dsp}}$	$f^0_{E_{agg}}$	ζ_l	φ_l	φ_b
eE3	4100	100	1875	2	0.51	0.965	0.9	0.15
eE6	6200	100	5076	2	0.37	0.965	0.9	0.15

Table 3. Resistance coefficients for the diffusion of PBS, dispersed and dissolved embelin, and for the dissolution of dispersed and agglomerated embelin.

	eE3	eE6
PBS diffusion	$\left(\frac{D_{Aq}}{[(e/2)\cdot(1-\zeta_l)]^2}\right)^{-1} = 2\cdot 10^3\ h$	
Diffusion of the dispersed embelin	$\left(\frac{D_{E_{dsp}}}{(e/2)^2}\right)^{-1} = 2\cdot 10^1\ h$	
Diffusion of the dissolved embelin	$\left(\frac{D_{E_o}}{[(e/2)\cdot(1-\zeta_l)]^2}\right)^{-1} = 2\cdot 10^{-3}\ h$	
Dissolution of dispersed embelin in PBS	$k'_{E_{dsp}}{}^{-1} = 3\cdot 10^{-4}\ h$	$k'_{E_{dsp}}{}^{-1} = 9\cdot 10^{-5}\ h$
Dissolution of agglomerated embelin in PBS	$k'_{E_{agg}}{}^{-1} = 1\cdot 10^{-1}\ h$	$k'_{E_{agg}}{}^{-1} = 4\cdot 10^{-2}\ h$

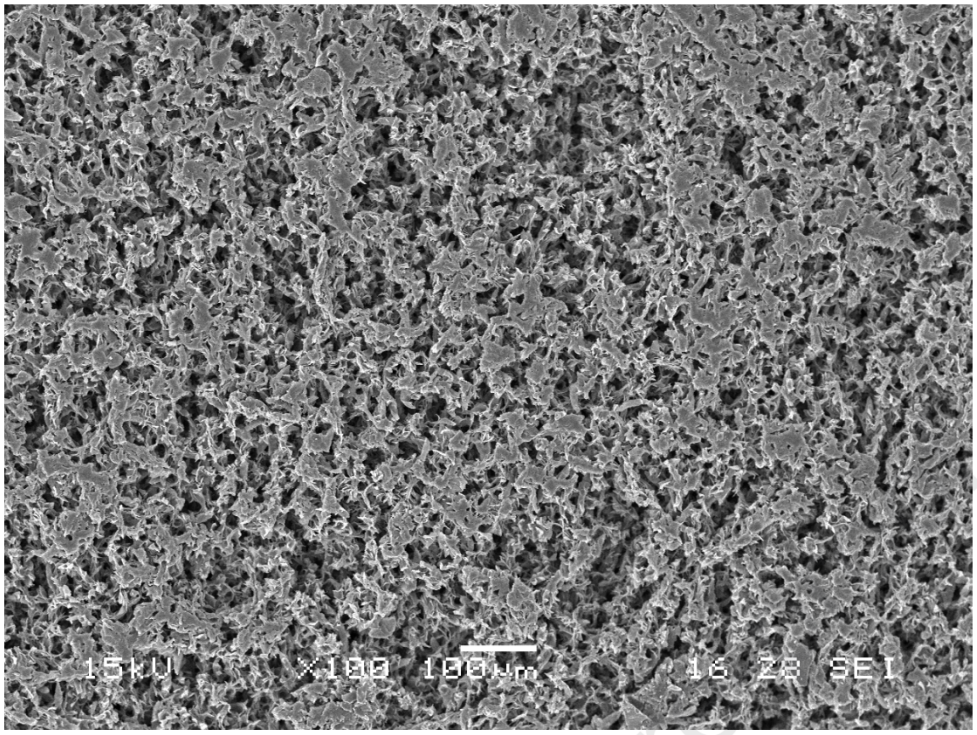

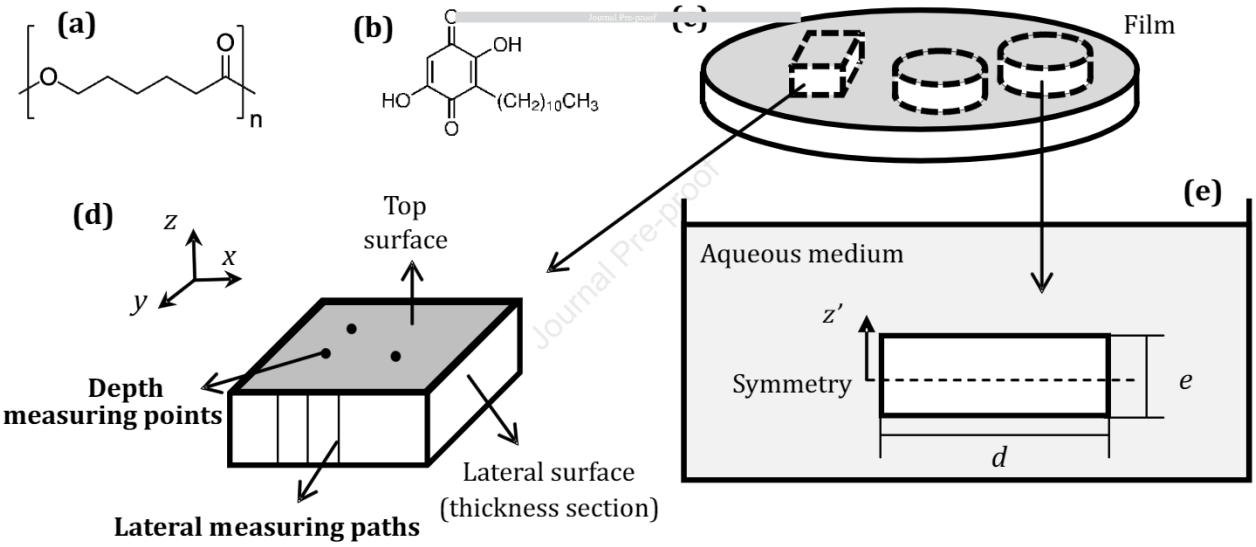

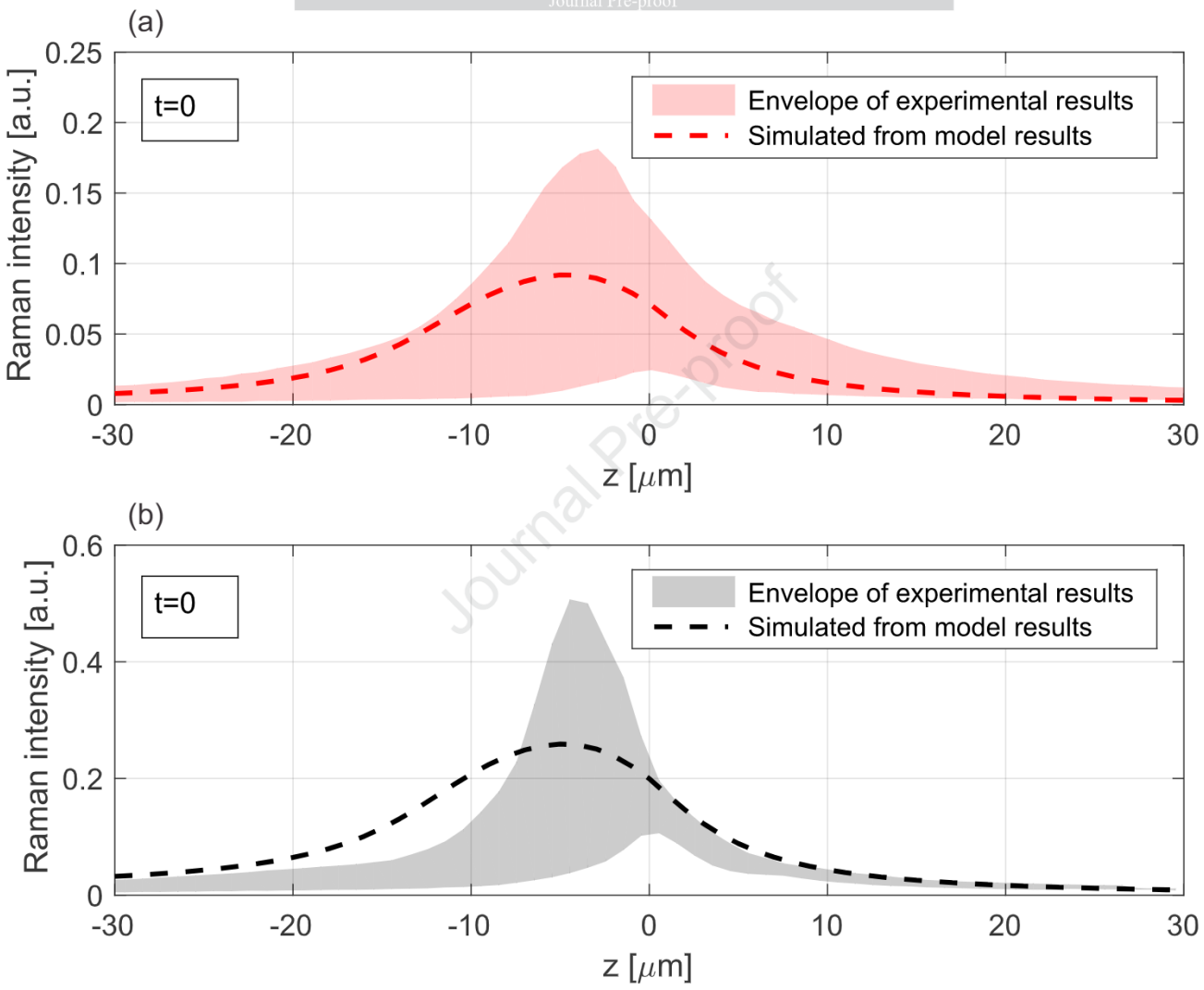

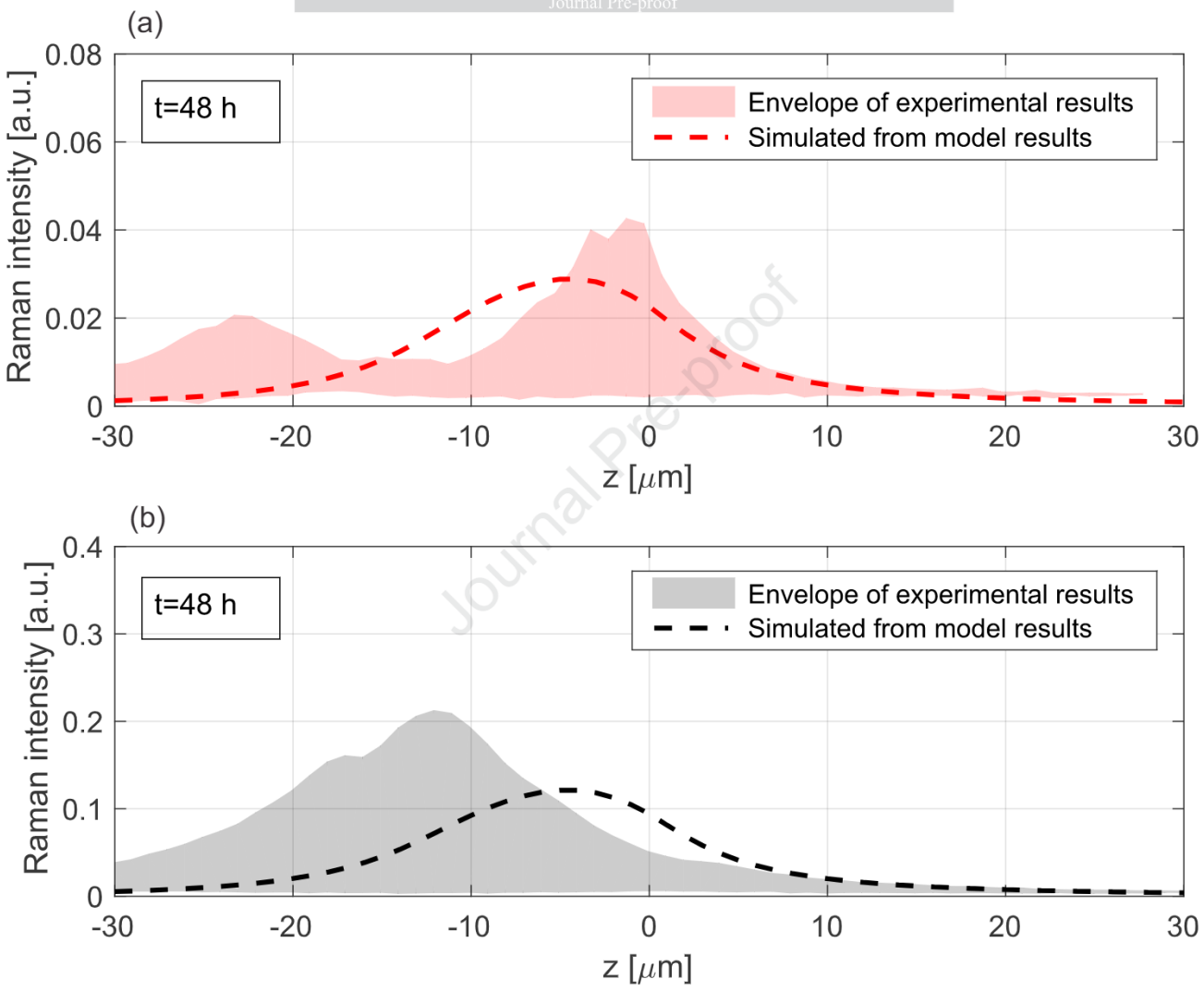

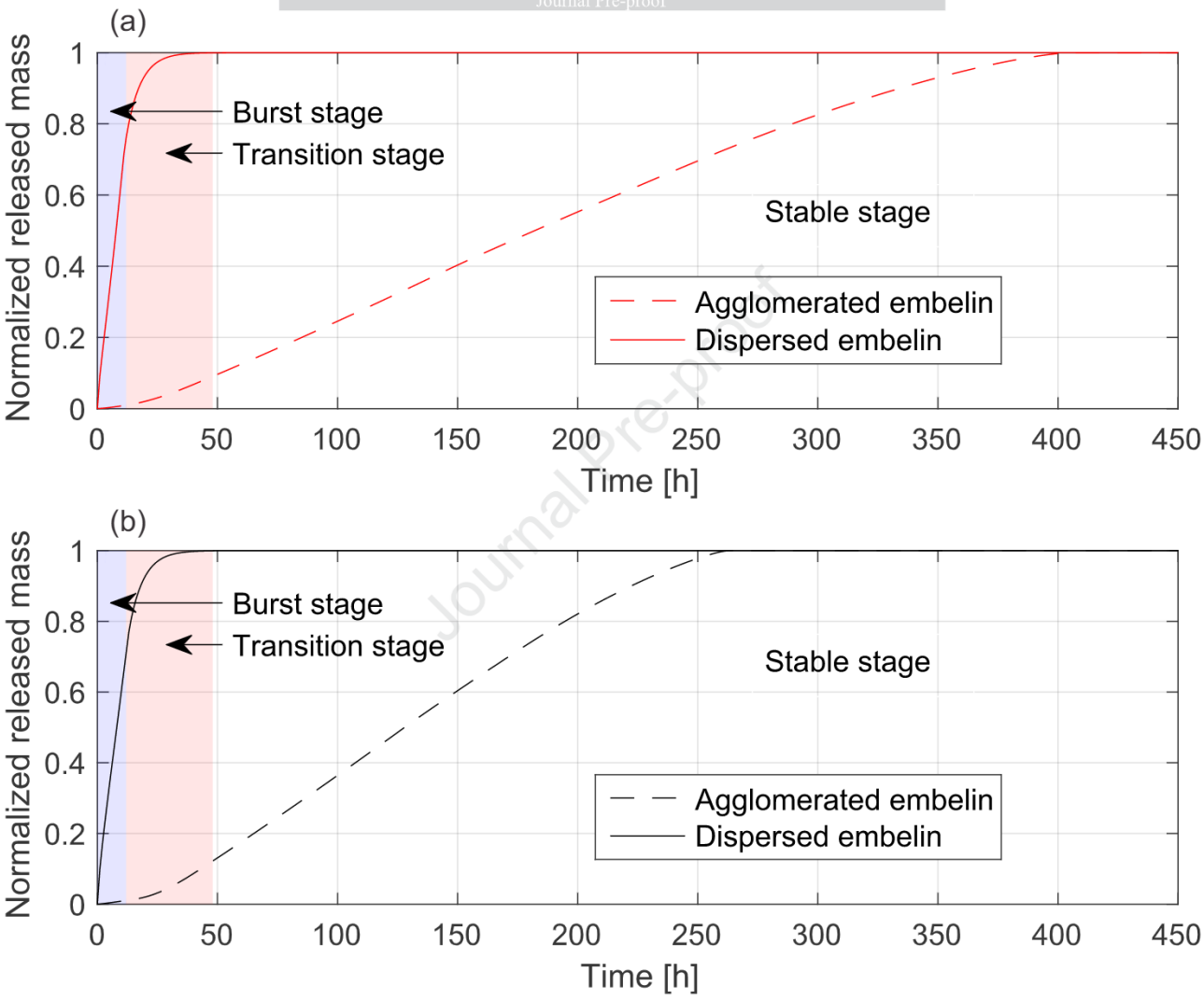

(a)

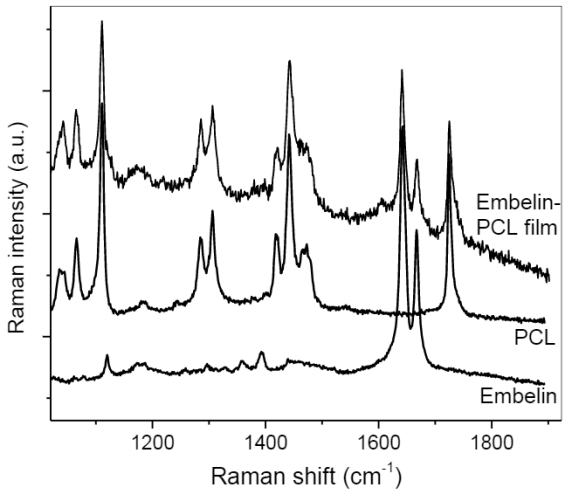

(b)

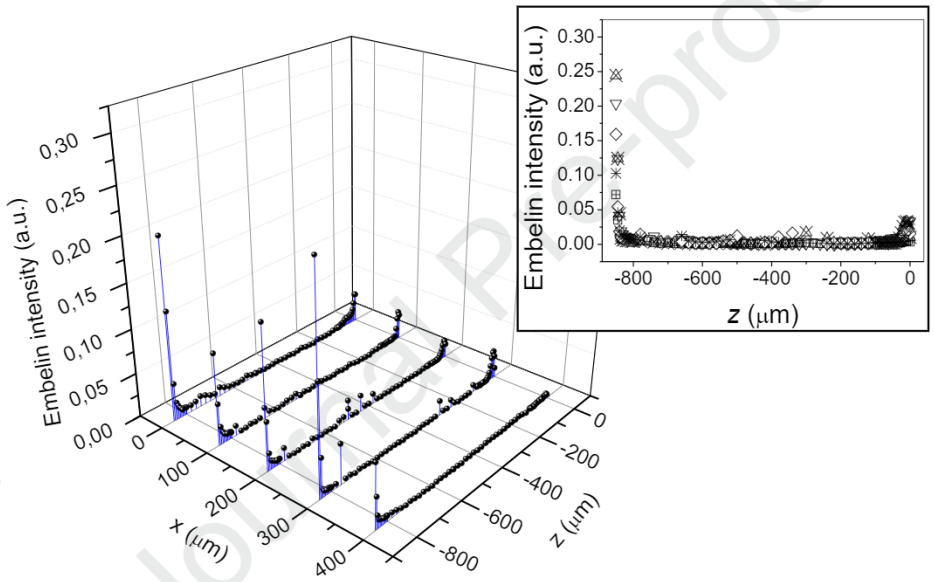

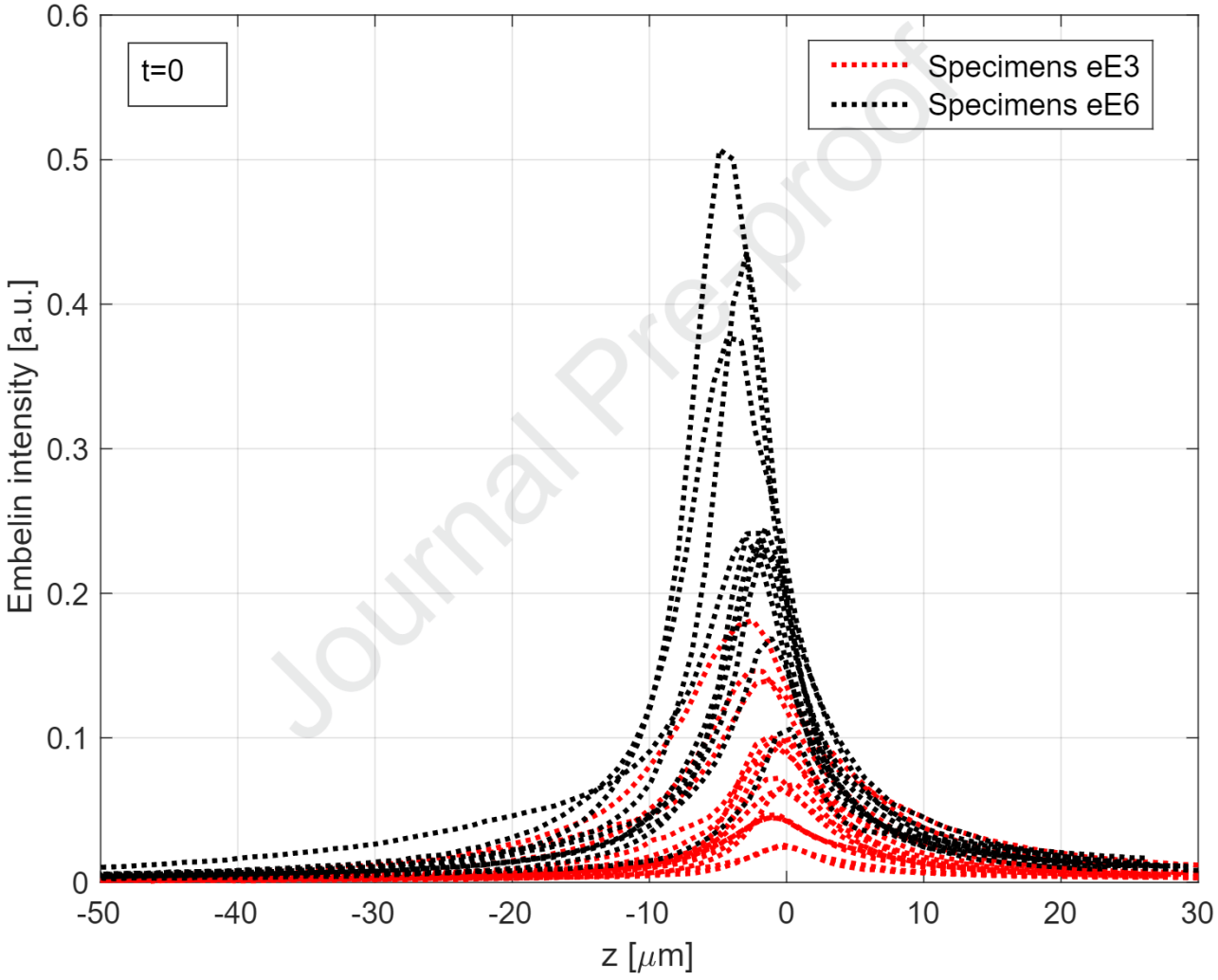

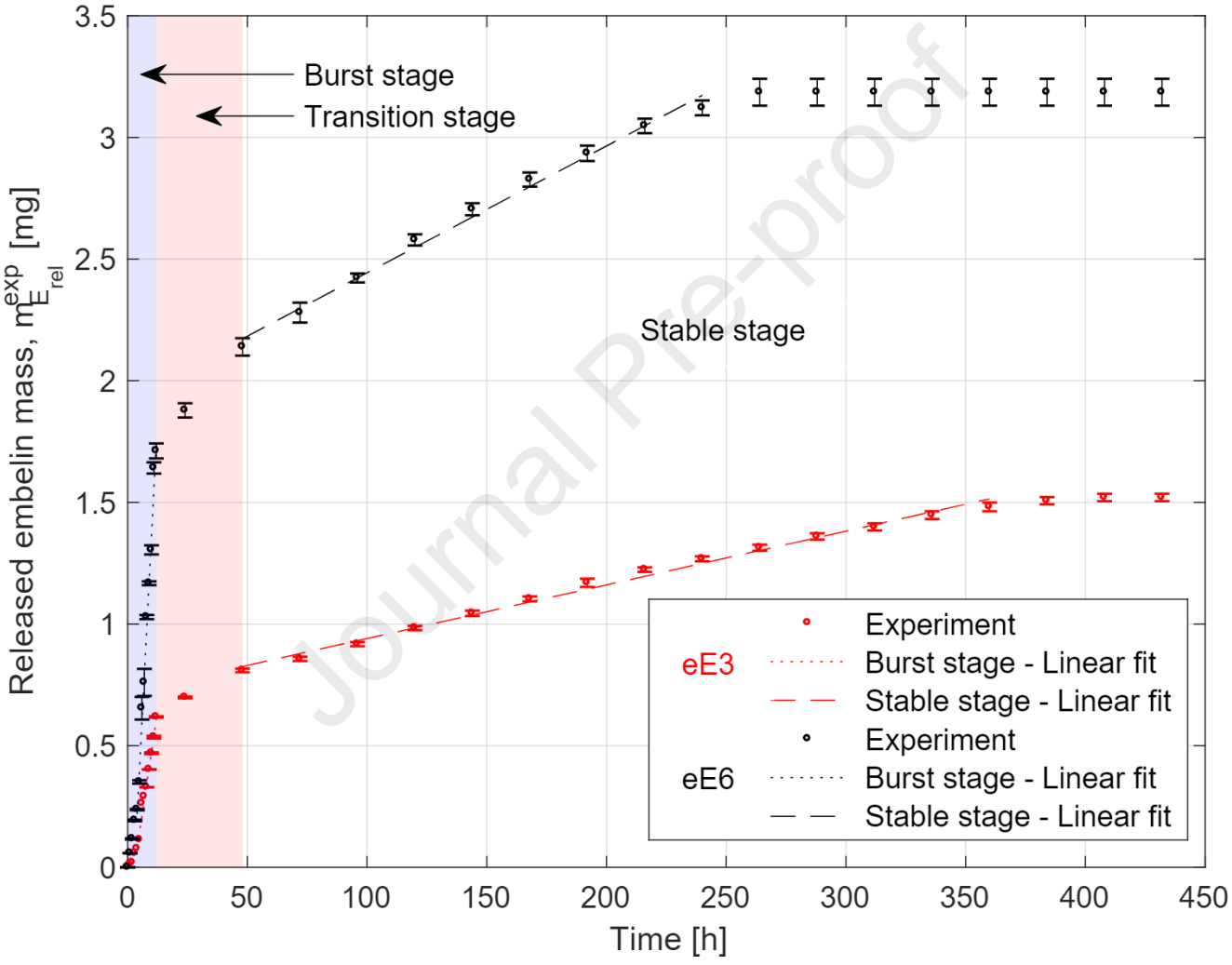

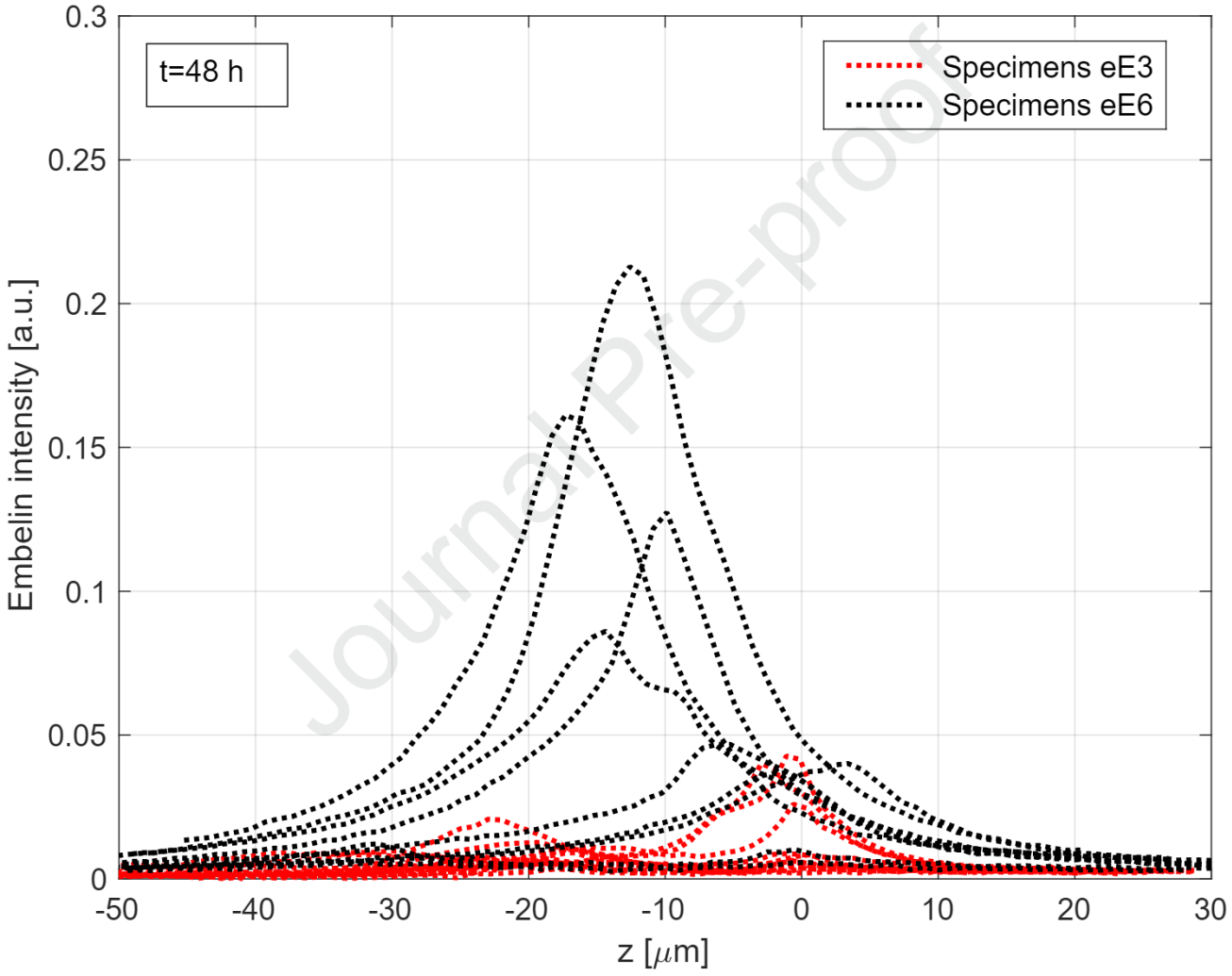

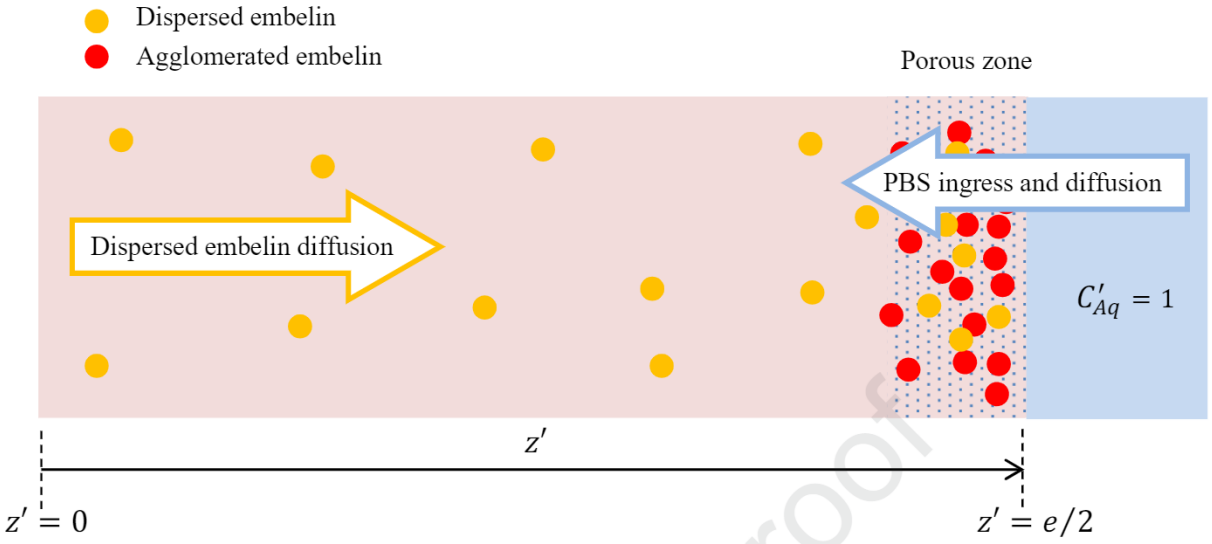

(*a*)

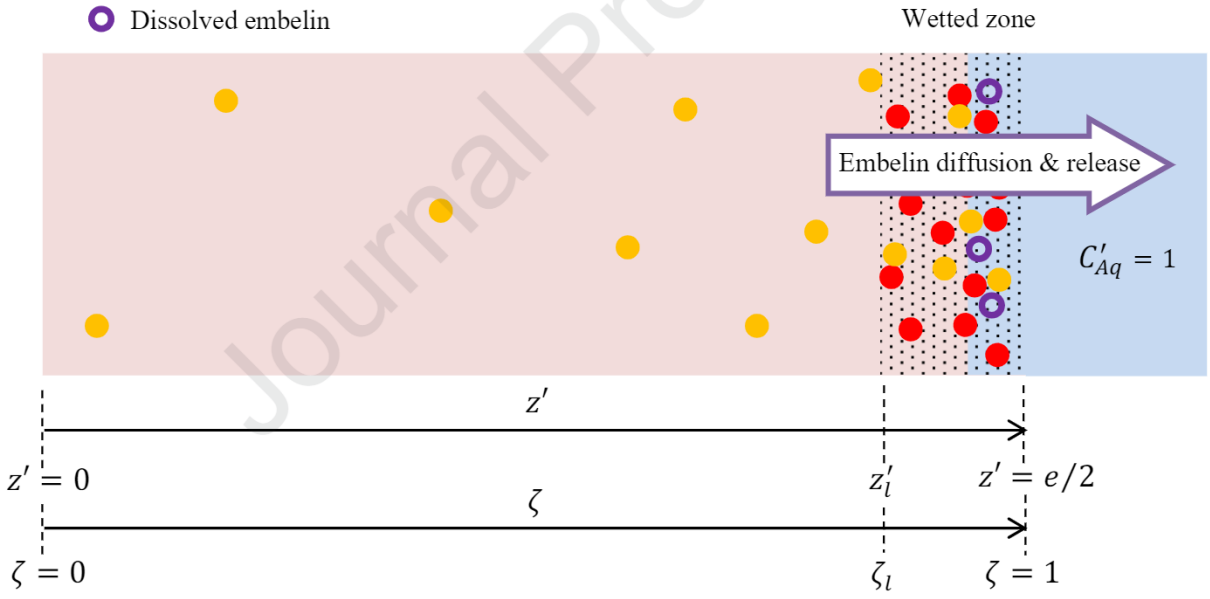

(*b*)

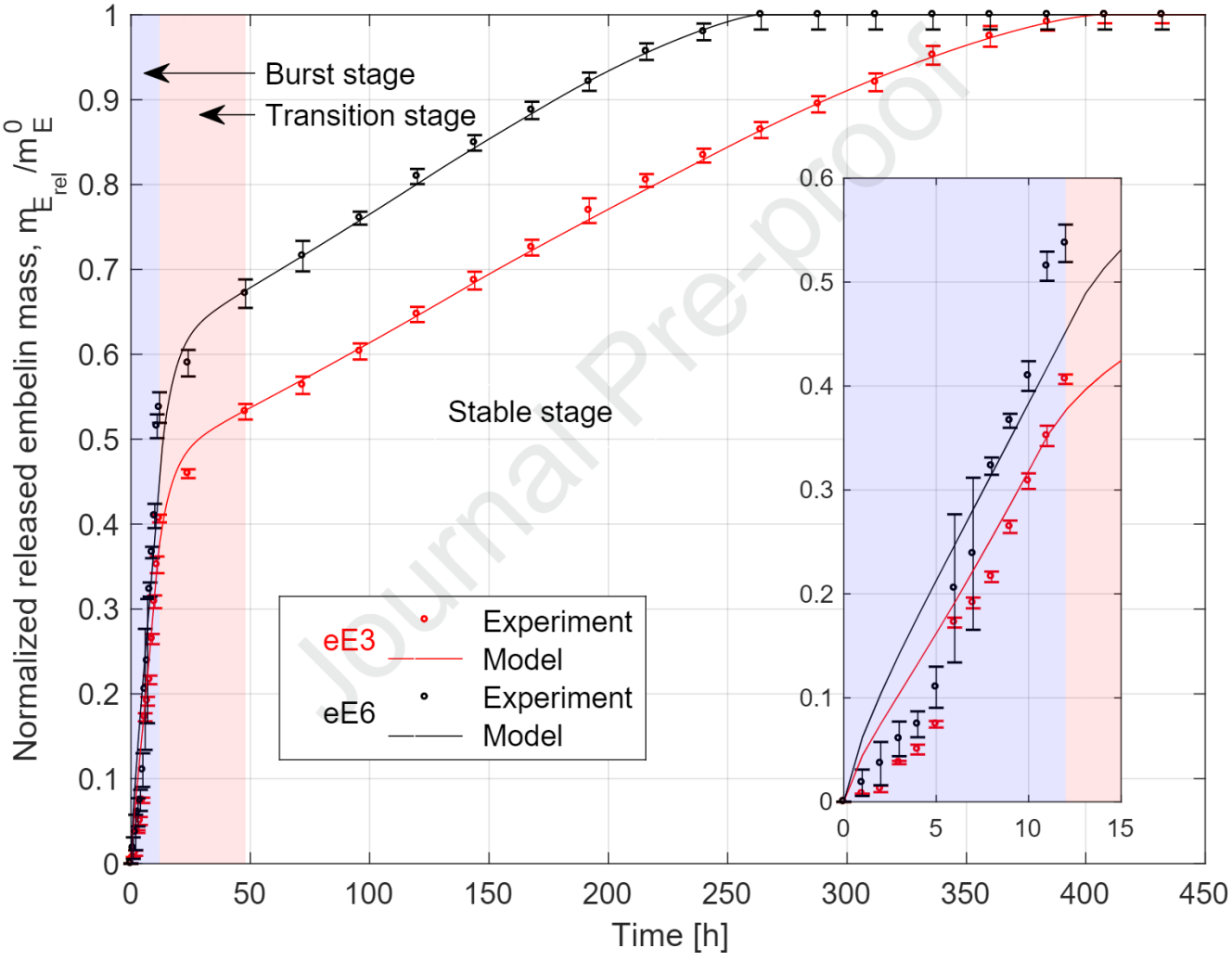

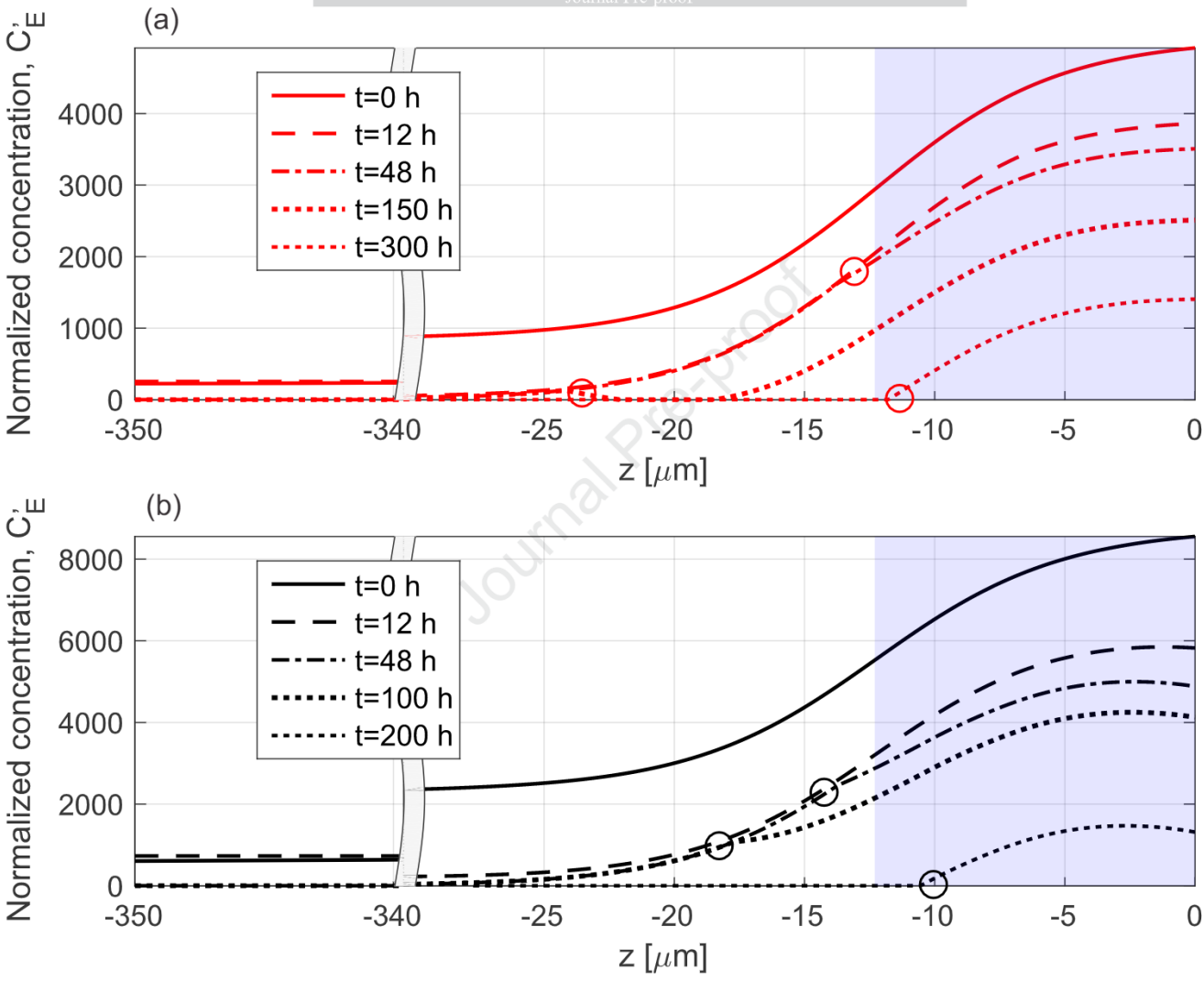

Highlights

- Embelin is released after being dissolved by the solution entering the sample.
- The solution diffusion coefficient is the critical parameter for the model tuning.
- Disperse embelin is liberated during the rapid initial release stage.
- Superficial agglomerated embelin is liberated during the long-lasting stable stage.
- Raman microscopy validates the model set-up and results.

CRediT author statement

Irene T. Seoane: Conceptualization, Investigation, Methodology, Formal analysis, Software, Validation, Writing. **Pablo R. Cortez Tornello:** Conceptualization, Investigation, Methodology, Formal analysis. **Leonel Silva:** Resources, Formal analysis. **Pablo Tomba:** Resources, Formal analysis. **Gustavo A. Abraham:** Conceptualization, Supervision. **Adrián Cisilino:** Conceptualization, Validation, Supervision, Visualization, Writing.

Declaration of interests: None

X The authors declare that they have no known competing financial interests or personal relationships that could have appeared to influence the work reported in this paper.

☐The authors declare the following financial interests/personal relationships which may be considered as potential competing interests: